האוניברסיטה העברית בירושלים-הפקולטה למתמטיקה ולמדעי הטבע

בית הספר להנדסה ולמדעי המחשב-המחלקה לפיסיקה יישומית

עבודת גמר לתואר מוסמך בנושא:

מוליך גלים פלסמוני בעל איבודים נמוכים בפלטפורמת סיליקון.

CMOS compatible Long-range dielectric-loaded surface plasmon-polariton waveguides (LR-DLSPPW)

מוגשת על ידי רועי זקצר

בהנחיית פרופסור אוריאל לוי

Acknowledgments

I would like to thank my advisor, Prof. Uriel Levy for his guidance and support throughout the time I was working on this research.
I would like to express my gratitude to Boris Desiatov, his advices and instructions helped me to advance my research.
I would like to thank Noa Mazurski for her guidance through the fabrication process.
The devices could not have been fabricated without the staff of the HUJI nano fabrication and characterization center.
Last but not least I would like to thank the NanoOpto group, mostly Alex Naiman, Liron Stern, Ilya Goykhman, Meir Grajower, Alexandros Emboras, Avner Yanai, Yoel Sebbag, Anat Szapiro, David Ohana, Avi Bakal, Yonatan Bar-David, Oren Lotan, Nir Kaplan and Eliran Talker for fruitful discussions, good advice, patience and fun.

Abstract

In the field of Silicon Integrated Nanophotonics it is our goal to implement nanoscale photonic circuits using well established manufacturing process of electronics devices. Achieving this goal will allow to integrate electrical and optical functionalities on the same chip. It will furthermore improve the yield and reduce the costs of photonic devices.

In order to reach this goal there is a need to propagate light on chip, to confine light to nanometric scale and to modulate data. In this respect, plasmonic waveguides are attracting growing attention in the last decade owing to their capability to confine light at the nanoscale and the availability of "built in" metal lines within the devices. A major drawback common to these waveguides is the high propagation loss which is a direct result of the ohmic loss in the metal. In contrast, silicon waveguides are able to propagate light significantly lower loss. Yet, silicon waveguides do not provide the easy contact reach that plasmonics offers.

Our proposed waveguide structure is known as Long Range –Dielectric Loaded Surface Plasmon Polariton Waveguide (LR-DLSPPW) because it supports a Long Range SPP mode. This is achieved by positioning a metal strip in a symmetric-like dielectric environment which results in minimization of the longitudinal electric field inside the metal and as result the effect of ohmic loss on the overall propagation loss of the device is significantly reduced. Our proposed waveguide consists of a Si3N4 rib waveguide, positioned on top of a thin metal strip, placed on oxidized Silicon on Insulator chip. The LR-DLSPPW offers the advantages of high confinement, high propagation length and easy contact reach.

The device was designed by finite-element method approach. It was fabricated using electron beam lithography, evaporation of aluminum, plasma enhanced chemical vapor deposition of Si3N4 and reactive ion etching. Finally, it was tested by near field scanning optical microscopy and transmission spectroscopy. The near-field optical microscopy characterization allowed us to verify the modes content. Losses were characterized by measuring the output transmission of light using several different length devices. The propagation length was ~ 1mm, which is compatible with the current state of the art in the field (mostly polymeric structure), yet offering the important advantage of being CMOS compatible platform. As such, the proposed device may be used as a building block in future on chip communication and information systems.

Table of contents

Contents

1. Introduction

This thesis describes the design, fabrication and measurement of a waveguide, consisting of both plasmonic and photonic properties. In this chapter we introduce the current technologies for propagating light on chip, provide the motivation for such a waveguide and present current waveguides that have similar properties. Finally, a short summary of the work is provided. .

1.1 Silicon photonics and plasmonics

1.1.1 Silicon photonics

The field of silicon photonics [1-2] is the study and the development of photonic components, devices and systems using silicon platform. In most cases, a relatively thin layer of silicon is positioned on top of a silicon oxide layer in what is known as the silicon on insulator (SOI) platform. SOI is used in the current semiconductor industry technology, which is Complementary Metal-Oxide-Semiconductor (CMOS), when complete isolation between the bulk silicon and the device is needed [3] .The fact that silicon is the main substrate in today electronics devices gives us the possibility to integrate photonic components inside and between microchips. These chips with optical and electrical functionalities can simplify the construction of routers and signal processors for optical communication [4-5]. As the microelectronics industry progress towards faster and denser chips a serious problem arises, which is interconnects density [6]. In today technology the length of interconnects per cm^2 is 6 kilometer which generates high power density and a major heat problem [7]. Silicon photonics can offer a solution to this problem by replacing the metal interconnects with waveguides [8-9]. Silicon has a refractive index of 3.46 which result in a sub micron effective wavelength and high confinement. The high confinement allows us to fabricate dense chips with multiple components. Propagating information in the form of light gives us the opportunity to use the wide bandwidth of optical communication. We can achieve this wide bandwidth through WDM multiplexing [10-11] and\or mode division multiplexing [12]. Besides propagating the signal from one point to another (core to memory, core to core) there is also a need to switch and modulate the signal. In order to switch and modulate we can use the thermo optic effect [13] or the carrier depletion effect [14] which modifies the refractive index of silicon. Both effects require the application of voltage which in turn requires the implementation of metal contacts. The problem with metal contacts in silicon photonics is ohmic losses. A common solution allowing for these losses to be minimized is by distancing the contacts from the waveguide. Unfortunately, this results in smaller tuning strength, higher power consumption and slower operation speeds as a consequent of the contacts high resistance. A promising technology in this respect is plasmonics [15].

1.1.2 Plasmonics

Surface Plasmons Polaritons (SPPs) are electromagnetic waves which travel along a metal-dielectric interface. Because the SPPwave propagates at the interface between metal and dielectric material we can apply voltage directly to the dielectric medium of the SPP resulting in lower power consumption and faster devices. Another advantage of SPPs is related to their short effective wavelength, resulted from the high momentum of electrons. Therefore, it is possible to confine light to the nanoscale [16], which can result in smaller and denser devices [17-28]. The high permittivity of metals in comparison to dielectric materials results in field enhancement in the dielectric medium, next to the interface between the metal and the dielectric material which can be exploited for devices based on nonlinear effects [29]. Interband excitation of non-equilibrium electrons in gold and aluminum results in changes in the imaginary part of the metal refractive index, and these qualities have been used to fabricate ultra fast plasmonics modulators [30-31]. Furthermore, the ability to propagate and confine light to the nanoscale made SPP a promising platform for bio-sensing and lab on chip devices [32-33]. On the downside, SPP major drawback is that by propagating on the surface of the metal, it is strongly influenced by the high ohmic losses and thus propagation distances as low as tens of microns are typically achieved. As a result, it is not straightforward to propagate a signal from one end of the chip to the other (typically several millimeters in length) by using plasmonics waveguides and it is also difficult to achieve high Q resonators which are needed for variety of applications such as filters, lasers and sensing to name a few.

1.2 Motivation for the LR-DLSPPW

Up to now we have presented two technologies. The first, silicon photonics, offers relatively long propagation length and good confinement of electromagnetic energy, but it cannot be integrated easily with metal contact. The second, plasmonics, offers nanoscale confinement, easy contact reach, and fast modulation but supports very short propagation distance. It could be useful to have a technology which combines both and allow us to navigate between nanoscale confinement and high losses to good confinement and low losses, to enjoy both worlds with as little as possible compromises.

1.3 Current state of the art

Hybrid waveguides [34-35] follow the above mentioned motivation. Typically, the hybrid structure consists of a high refractive index medium that is separated from a metal surface by a thin gap of low refractive index spacer. In this configuration, the electromagnetic energy resides in both the high and the low index materials and the guiding mechanism has characteristics of plasmonic and photonic modes which are coupled. As a result, by controlling the dimensions of the gap and the parameters of the high refractive index layer, the mode can be varied from photonic to plasmonic regime, allowing longer

propagation length than a plasmonic waveguide. In [22] a hybrid waveguide was used to reduce the ohmic losses so it could be used as a laser cavity. The high confinement of hybrid waveguides with low losses was used to design small microring resonators with high Q factors for sensing [36].Hybrid structures can produce modes with high field intensity, consequently producing high nonlinear effects for optical parametric amplifiers [37]. Hybrid waveguides can also be used for fast and power efficient phase modulators [37]. Another structure that can provide easy metal connection with reasonable propagation length is the Long Range Dielectric loaded Surface Plasmons Polaritons Waveguides [39-40]. The LR-DLSPPW consists of dielectric ridge deposited on a thin metal strip which is placed on a dielectric slab positioned on a lower index substrate. The goal of this structure is to create a semi-symmetrical dielectric environment around the metal strip which allows formation of a long range SPP mode. Recently, a high index CMOS compatible LR-DLSPPW has been proposed and analyzed [41].

1.4 Summary

In this work we experimentally demonstrate the design, fabrication and the characterization of a CMOS compatible LR-DLSPPW. Following the fabrication process we have measured the propagation loss of the LR-DLSPPW by measuring the transmission of light through of several devices with different sizes. Using Near field Scanning Optical Microscope we have verified the modes content. The demonstrated structure supports the propagation of both light, with reasonable propagation length of ~700[um], and electrical signals. The electrical signal in the metal can be used to control the propagation of light, e.g. by the thermo-optic effect or electro-optic effect.

2. Theoretical background

In this chapter we explain the main idea of wave guiding starting from electromagnetic waves, proceeding to basic waveguide structures including the surface plasmons polaritons (SPP) guiding mechanism. We also explain the method of simulation, the theory behind coupling light in to a waveguide and how near field optics is helpful in characterizing our waveguide structures.

2.1 Electromagnetic waves

2.1.1 Wave equation

The relations between the electric current density $\vec{J}$, the electric charge density ρ, the magnetic field $\vec{\mathrm{B}}$ and the electric field $\vec{\mathrm{E}}$ are described by Maxwell equations [42]:

$$\vec{\nabla}\cdot E = \frac{\rho}{\varepsilon}$$

$$\vec{\nabla}\times\vec{E} = -\frac{\partial\vec{B}}{\partial t} \quad (1)$$

$$\vec{\nabla}\cdot\vec{B} = 0$$

$$\vec{\nabla}\times B = \mu_0\vec{J} + \varepsilon\mu_0\frac{\partial E}{\partial t} \quad (2)$$

(3)

(4)

Assuming the electric and magnetic fields propagate in vacuum, there is no charge or current density so we can place $\rho = 0, \mathrm{J} = 0$ and rewrite Maxwell equations as:

$$\vec{\nabla}\cdot E = 0$$

$$\vec{\nabla}\times(\vec{\nabla}\times E) = -\frac{\partial}{\partial t}\vec{\nabla}\times\vec{B} \quad (5)$$

$$\vec{\nabla}\cdot\vec{B} = 0 \quad (6)$$

$$\frac{\partial}{\partial t}\vec{\nabla}\times B = \varepsilon_0\mu_0\frac{\partial^2 E}{\partial t^2} \quad (7)$$

(8)

Where μ_0 and ε_0 are the permeability and permittivity in vacuum. From eq.5-6, 8 we can obtain the wave equation for the electric field:

$$\vec{\nabla}\times(\vec{\nabla}\times\vec{E}) = \vec{\nabla}\left(\vec{\nabla}\cdot\vec{E}\right) - \vec{\nabla}^2\vec{E} = -\varepsilon\mu_0\frac{\partial^2 E}{\partial t^2} \quad (9)$$

By placing eq.5 in eq.9 we get:

10. $\vec{\nabla}^2\vec{E} = \varepsilon\mu_0 \frac{\partial^2 E}{\partial t^2}$

In a similar way we can obtain the wave equation for the magnetic field

$$\vec{\nabla}\times\vec{E} = -\frac{\partial\vec{B}}{\partial t}$$

12. $\vec{\nabla}\times\left(\vec{\nabla}\times\vec{B}\right) = \varepsilon\mu_0 \frac{\partial}{\partial t}\vec{\nabla}\times\vec{E}$
11.

13. $\vec{\nabla}^2\vec{B} = \varepsilon\mu_0 \frac{\partial^2\vec{B}}{\partial t^2}$

As we know $\varepsilon_0\mu_0 = \frac{1}{c^2}$ where c is the speed of light in vacuum, so eq.13 can be rewritten as

14. $\vec{\nabla}^2\vec{B} = \frac{1}{c^2}\frac{\partial^2\vec{B}}{\partial t^2}$

One of the solutions to eq.14is the travelling plane wave

15. $\vec{\mathrm{E}} = \vec{\mathrm{E}}(\vec{\mathrm{k}}\cdot\vec{\mathrm{r}} - \omega\mathrm{t})$

By placing eq.15 to the wave equation we get that

16. $|\mathrm{k}| = \frac{\omega}{\mathrm{c}} = \frac{2\pi}{\lambda}$

Which is known as the dispersion relation of a wave in free space.

We shall now examine the relationship between E, B and k, from eq.11 we receive

$$\left(\vec{\nabla}\times\vec{E}\right)_x = \frac{\partial E_z}{\partial y} - \frac{\partial E_y}{\partial \mathrm{z}} = k_y \frac{\partial E_z}{\partial\left((\vec{k}\cdot\vec{r} - \omega t)\right)} - k_z \frac{\partial E_y}{\partial(\vec{k}\cdot\vec{r} - \omega t)} = \left(\vec{k}\times\frac{\partial E}{\partial(\vec{k}\cdot\vec{r} - \omega t)}\right)_x \Rightarrow$$

17.
18. $\vec{\nabla}\times\vec{E} = \vec{k}\times\frac{\partial E}{\partial(\vec{k}\cdot\vec{r} - \omega t)}$

Applying eq.17 and eq.18 in to eq.1-4 we get

$$\vec{k}\times\frac{\partial\vec{E}}{\partial(\vec{k}\cdot\vec{r} - \omega t)} = \omega\frac{\partial\vec{B}}{\partial(\vec{k}\cdot\vec{r} - \omega t)}$$

19.

$$\vec{k} \times \frac{\partial \vec{B}}{\partial(\vec{k}\cdot\vec{r}-\omega t)} = -\omega\varepsilon\mu_0 \frac{\partial \vec{E}}{\partial(\vec{k}\cdot\vec{r}-\omega t)}$$

20.

If we neglect field constants in space integration, eq.19 will give us

21. $\vec{k} \times \vec{E} = c\vec{B}$

E, B and k create a right hand trio. In the case of plane wave, E and B are in phase and both are perpendicular to the wave vector k.

2.1.2 Snell law

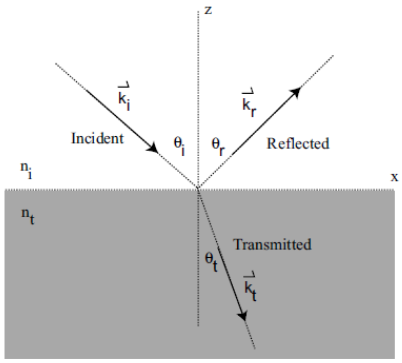

Figure.1 Plane wave incident upon a plane boundary separating two materials

Consider a plane wave incident upon a plane boundary separating two materials (Figure.1). There will be a reflected wave and a transmitted wave.

$$E_i = e^{i(k_i\cdot r-\omega t)}$$

22. $E_r = e^{i(k_r\cdot r-\omega t)}$

$$E_t = e^{i(k_t\cdot r-\omega t)}$$

The phase in the three waves in the incident should be equal so we can deduce that:

23. $\vec{k}_i\cdot\vec{r}\big|_{z=0} = \vec{k}_r\cdot\vec{r}\big|_{z=0} = \vec{k}_t\cdot\vec{r}\big|_{z=0}$

From eq.23 we deduce

24. $n_i\left(k_x^i x + k_y^i y\right) = n_i\left(k_x^r x + k_y^r y\right) = n_t\left(k_x^t x + k_y^t y\right)$

Eq.24 is true for the entire plane so:

$$k_x^i = k_x^r, k_y^i = k_y^r$$

$$k_x^i = \left(\frac{n_t}{n_i}\right) k_x^t, k_y^i = \left(\frac{n_t}{n_i}\right) k_y^r =>$$

25. $n_i \sin\theta_i = n_t \sin\theta_t$

If the transmitted angle is larger than 90 degrees we have the case of total internal reflection, in order for this to occur the incident angle must be larger than the critical angle:

26. $\theta_{crit} = \sin^{-1}\left(\frac{n_t}{n_i}\right)$

2.1.3 Boundary conditions

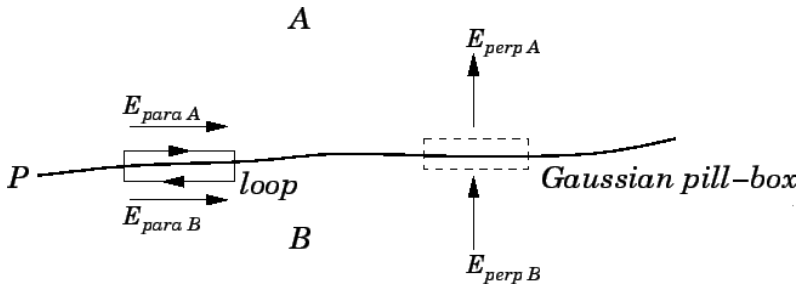

Figure.2 Interface between two materials A and B.

Consider an interface P between two media A and B (Figure.2), we first apply the Gauss' law to a Gaussian pill-box with cross section A, assuming the box is parallel to the interface and its sides length close to zero we can write

27. $$\int_S E \cdot dS = \frac{1}{\varepsilon_0}\int_V \rho dV => \left(E_{\perp A} - E_{\perp B}\right) A = \frac{1}{\varepsilon_0}\sigma A => E_{\perp A} - E_{\perp B} = \frac{\sigma}{\varepsilon_0}$$

We apply the Faraday's law to a rectangular loop C, whose sides are parallel to the interface.

28. $$\int_C E \cdot dl = -\frac{\partial}{\partial t}\int_S B dS => \left(E_{\parallel A} - E_{\parallel B}\right) l = -\frac{\partial}{\partial t} B_\perp A$$

Again we assume very small sides so $A \to 0$ and

29. $$E_{\|A} - E_{\|B} = 0 \Rightarrow E_{\|A} = E_{\|B}$$

In the same way by applying Ampere's Law and assuming there aren't any surface currents we get

30. $$H_{\|A} - H_{\|B} = 0$$

By applying Gauss' law we get

31. $$\int_S B \cdot dS = 0 \Rightarrow \mu_a H_{\perp A} - \mu_b H_{\perp B} = 0$$

2.2 Waveguides

As previously mentioned, our device is dielectric loaded waveguide. In this section we will explore the basic waveguides starting with a slab waveguide**.**

2.2.1 Slab waveguide

In order to gain basic understanding of how a waveguide works it is sufficient to consider a high index slab sandwiched between two lower indexes slabsFigure.3). Snell's law (26) shows us that at certain angels we get total internal reflection:

Figure.3 Illustration of a symmetrical three layer slabs waveguide with two wave fronts propagating in it.

In order to achieve constructive interference between two wave fronts that the following condition should be satisfied:

32. $$\frac{2\pi}{\lambda}(2d\cos\theta) = 2\pi m$$

This condition is fulfilled only at a certain discrete angels. These angles are given by:

$$\cos\theta = \mathrm{m}\frac{\lambda}{2\mathrm{d}} \quad (33.)$$

As can be seen, the smaller θ_c the smaller d can be. We now consider the general case of a slab waveguide by solving the wave equation. Slab waveguide can consists of several layers of materials with different dielectric constants and straight parallel and infinite interfaces (Figure.4).

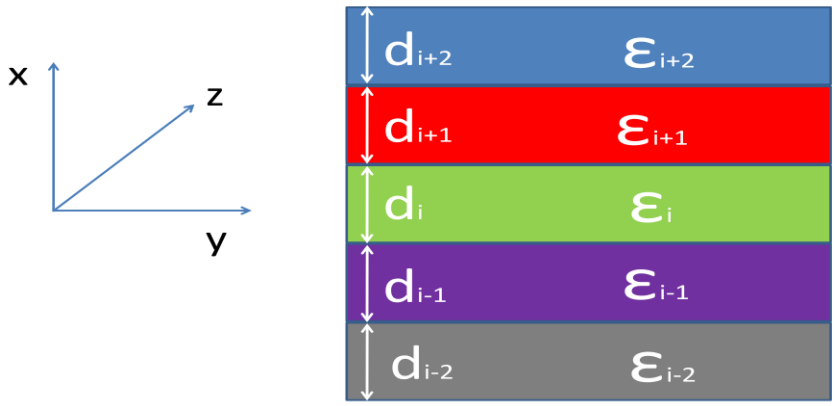

Figure.4Illustration of a Slab wave guide consisting of multiple layers with different permittivities and different widths.

We assume a solution of a wave propagating in the z direction. This assumption will hold though the entire thesis.

$$E = E(x,y)e^{j(\omega t-\beta z)} \quad (34.)$$

$$H = H(x,y)e^{j(\omega t-\beta z)} \quad (35.)$$

Maxwell's equations (eq.1-4)can be separated into two sets of equations that give two sets of solutions

Assuming the field does not change in the y direction we get

Maxwell	Transverse Magnetic	Transverse Electric
$\vec{\nabla}\times\vec{E}=-\mu_0\frac{\partial\vec{H}}{\partial t}$	$j\beta E_x-\frac{\partial E_z}{\partial x}=-j\omega\mu_0 H_y$	$\beta E_y=-\omega\mu_0 H_x$
		$\frac{\partial E_y}{\partial x}=-\mu_0 j\omega H_z$
$\vec{\nabla}\times H=\varepsilon_0 n^2\frac{\partial E}{\partial t}$	$j\beta H_y=j\omega\varepsilon_0 n^2 E_x$	$-j\beta H_x-\frac{\partial H_z}{\partial x}=j\omega\varepsilon_0 n^2 E_y$
	$\frac{\partial H_y}{\partial x}=j\omega\varepsilon_0 n^2 E_z$	

From the TM side we get the following wave equation

$$-\frac{\partial^2 H_y}{\partial x^2}=H_y\left(k^2n^2-\beta^2\right)$$

And from the TE side we get the following wave equation

36.

$$\frac{\partial^2 E_y}{\partial x^2}=E_y\left(\beta^2-k^2n^2\right)$$

37.

Assuming a general solution of:

38. $E_{yi}=\left(A_i e^{-k_{xi}(x-x_{i-1})}+B_i e^{k_{xi}(x-x_{i-1})}\right)e^{-j\beta z}, k_{xi}=\sqrt{\beta^2-\varepsilon_i k_0^2}$

39. $H_{yi}=\left(A_i e^{-k_{xi}(x-x_{i-1})}+B_i e^{k_{xi}(x-x_{i-1})}\right)e^{-j\beta z}, k_{xi}=\sqrt{\beta^2-\varepsilon_i k_0^2}$

Every boundary gives us two equations due to the continuity of the tangents fields. For TE:

$$E_{yi}^{+}=E_{yi}^{-}=>A_i e^{-k_{xi}(d_i)}+B_i e^{k_{xi}(d_i)}=A_{i+1}+B_{i+1}$$
$$H_{zi}^{+}=H_{zi}^{-}=>\left(-k_{xi}A_i e^{-k_{xi}(d_i)}+k_{xi}B_i e^{k_{xi}(d_i)}\right)=\left(-k_{xi+1}A_{i+1}+k_{xi+1}B_{i+1}\right)$$

This results in a transmission matrix:

40. $$\begin{pmatrix} A_{i+1} \\ B_{i+1} \end{pmatrix} = \frac{1}{2}\begin{pmatrix} e^{-k_{xi}(d_i)}\left(\frac{k_{xi}}{k_{xi+1}}+1\right) & e^{k_{xi}(d_i)}\left(1-\frac{k_{xi}}{k_{xi+1}}\right) \\ e^{-k_{xi}(d_i)}\left(1-\frac{k_{xi}}{k_{xi+1}}\right) & e^{k_{xi}(d_i)}\left(\frac{k_{xi}}{k_{xi+1}}+1\right) \end{pmatrix}\begin{pmatrix} A_i \\ B_i \end{pmatrix} =>$$

$$\begin{pmatrix} A_N \\ B_N \end{pmatrix} = T_{N-1}...T_4T_3T_2T_1\begin{pmatrix} A_1 \\ B_1 \end{pmatrix} => \begin{pmatrix} A_N \\ B_N \end{pmatrix} = \begin{pmatrix} t_{11} & t_{12} \\ t_{21} & t_{22} \end{pmatrix}\begin{pmatrix} A_1 \\ B_1 \end{pmatrix}$$

Assuming exponential decay in the first and last boundaries we get $t_{22} = 0$

For the simple structure of three slabs where the middle slab is with the highest refractive index

$$\begin{pmatrix} A_{i+2} \\ B_{i+2} \end{pmatrix} = \frac{1}{4}\begin{pmatrix} e^{-k_{x+1}(d_{i+1})}\left(\frac{k_{xi+1}}{k_{xi+2}}+1\right) & e^{k_{xi+1}(d_{i+1})}\left(1-\frac{k_{xi+1}}{k_{xi+2}}\right) \\ e^{-k_{xi+1}(d_{i+1})}\left(1-\frac{k_{xi+1}}{k_{xi+2}}\right) & e^{k_{xi+1}(d_{i+1})}\left(\frac{k_{xi+1}}{k_{xi+2}}+1\right) \end{pmatrix}\begin{pmatrix} e^{-k_{xi}(d_i)}\left(\frac{k_{xi}}{k_{xi+1}}+1\right) & e^{k_{xi}(d_i)}\left(1-\frac{k_{xi}}{k_{xi+1}}\right) \\ e^{-k_{xi}(d_i)}\left(1-\frac{k_{xi}}{k_{xi+1}}\right) & e^{k_{xi}(d_i)}\left(\frac{k_{xi}}{k_{xi+1}}+1\right) \end{pmatrix}\begin{pmatrix} A_i \\ B_i \end{pmatrix} =>$$

$$t_{22} = e^{-k_{xi+1}(d_{i+1})}\left(1-\frac{k_{xi+1}}{k_{xi+2}}\right)e^{k_{xi}(d_i)}\left(1-\frac{k_{xi}}{k_{xi+1}}\right) + e^{k_{xi+1}(d_{i+1})}\left(\frac{k_{xi+1}}{k_{xi+2}}+1\right)e^{k_{xi}(d_i)}\left(\frac{k_{xi}}{k_{xi+1}}+1\right) = 0$$

$$\beta^2 - \varepsilon_{i+1}k_0^2 < 0, \beta^2 - \varepsilon_i k_0^2, \beta^2 - \varepsilon_{i+2}k_0^2 > 0 => k_{xi+1} = jk_{xi+1}'$$

$$\left(\frac{k_{xi}}{k_{xi+2}}+1\right)\left(e^{k_{xi+1}(d_{i+1})} + e^{-k_{xi+1}(d_{i+1})}\right) + \left(-\frac{k_{xi+1}'}{jk_{xi+2}} + \frac{k_{xi}}{jk_{xi+1}'}\right)\left(e^{k_{xi+1}(d_{i+1})} - e^{-k_{xi+1}(d_{i+1})}\right) = 0$$

This gives us the mode equation:

$$\tan\left((d_{i+1})k_{xi+1}'\right) = \frac{-\left(k_{xi}+k_{xi+2}\right)k_{xi+1}'}{\left(-k_{xi+1}'^2 + k_{xi}k_{xi+2}\right)}$$

Solving it will give us discrete propagation constants (β). Applying them to our general solution will result in specific modes with their profiles.

41. For TM the tangential fields are H_y, E_z and the transmission matrix is:

42. $$\begin{pmatrix} A_{i+1} \\ B_{i+1} \end{pmatrix} = \frac{1}{2}\begin{pmatrix} e^{-k_{xi}(d_i)}\left(1+\frac{\varepsilon_{i+1}}{\varepsilon_i}\frac{k_{xi}}{k_{xi+1}}\right) & e^{k_{xi}(d_i)}\left(1-\frac{\varepsilon_{i+1}}{\varepsilon_i}\frac{k_{xi}}{k_{xi+1}}\right) \\ e^{-k_{xi}(d_i)}\left(1-\frac{\varepsilon_{i+1}}{\varepsilon_i}\frac{k_{xi}}{k_{xi+1}}\right) & e^{k_{xi}(d_i)}\left(1+\frac{\varepsilon_{i+1}}{\varepsilon_i}\frac{k_{xi}}{k_{xi+1}}\right) \end{pmatrix}\begin{pmatrix} A_i \\ B_i \end{pmatrix}$$

For the simple structure of three layers:

$$\begin{pmatrix} A_{i+2} \\ B_{i+2} \end{pmatrix} = \frac{1}{4} \begin{pmatrix} e^{-k_{xi+1}(d_{i+1})}\left(1+\frac{\varepsilon_{i+2}k_{xi+1}}{\varepsilon_{i+1}k_{xi+2}}\right) & e^{k_{xi+1}(d_{i+1})}\left(1-\frac{\varepsilon_{i+2}k_{xi+1}}{\varepsilon_{i+1}k_{xi+2}}\right) \\ e^{-k_{xi+1}(d_{i+1})}\left(1-\frac{\varepsilon_{i+2}k_{xi+1}}{\varepsilon_{i+1}k_{xi+2}}\right) & e^{k_{xi+1}(d_{i+1})}\left(1+\frac{\varepsilon_{i+2}k_{xi+1}}{\varepsilon_{i+1}k_{xi+2}}\right) \end{pmatrix} \begin{pmatrix} e^{-k_{xi}(d_i)}\left(1+\frac{\varepsilon_{i+1}k_{xi}}{\varepsilon_i k_{xi+1}}\right) & e^{k_{xi}(d_i)}\left(1-\frac{\varepsilon_{i+1}k_{xi}}{\varepsilon_i k_{xi+1}}\right) \\ e^{-k_{xi}(d_i)}\left(1-\frac{\varepsilon_{i+1}k_{xi}}{\varepsilon_i k_{xi+1}}\right) & e^{k_{xi}(d_i)}\left(1+\frac{\varepsilon_{i+1}k_{xi}}{\varepsilon_i k_{xi+1}}\right) \end{pmatrix} \begin{pmatrix} A_i \\ B_i \end{pmatrix}$$

$$T_{22} = e^{-k_{xi+1}(d_{i+1})}\left(1-\frac{\varepsilon_{i+2}}{\varepsilon_{i+1}}\frac{k_{xi+1}}{k_{xi+2}}\right)e^{k_{xi}(d_i)}\left(1-\frac{\varepsilon_{i+1}}{\varepsilon_i}\frac{k_{xi}}{k_{xi+1}}\right)+e^{k_{xi+1}(d_{i+1})}\left(1+\frac{\varepsilon_{i+2}}{\varepsilon_{i+1}}\frac{k_{xi+1}}{k_{xi+2}}\right)e^{k_{xi}(d_i)}\left(1+\frac{\varepsilon_{i+1}}{\varepsilon_i}\frac{k_{xi}}{k_{xi+1}}\right)=0$$

This gives us the mode equation:

$$e^{-2k_{xi+1}(d_{i+1})} = -\frac{\left(\varepsilon_i\varepsilon_{i+1}k_{xi+1}k_{xi+2}+\varepsilon_{i+1}k_{xi}k_{xi+2}\varepsilon_{i+1}+\varepsilon_{i+2}k_{xi+1}\varepsilon_i k_{xi+1}+\varepsilon_{i+2}k_{xi}\varepsilon_{i+1}k_{xi+1}\right)}{\left(\varepsilon_{i+1}\varepsilon_i k_{xi+1}k_{xi+2}-\varepsilon_{i+1}k_{xi}k_{xi+2}\varepsilon_{i+1}-k_{xi+1}\varepsilon_i k_{xi+1}\varepsilon_{i+2}+k_{xi}k_{xi+1}\varepsilon_{i+1}\varepsilon_{i+2}\right)} \quad \underline{43.}$$

For the simple case of a symmetric slab eq.43 reduces to

$\varepsilon_i = \varepsilon_{i+2} \Rightarrow k_{xi+2} = k_{xi} \Rightarrow$

$$\tanh(k_{xi+1}(\frac{d_{i+1}}{2})) = -\frac{\varepsilon_i k_{xi+1}}{\varepsilon_{i+1}k_{xi}} \quad \underline{44.}$$

$$\tanh(k_{xi+1}(\frac{d_{i+1}}{2})) = -\frac{\varepsilon_{i+1}k_{xi}}{\varepsilon_i k_{xi+1}}$$

2.2.2 General wave guide

We now look at a more general case where a high refractive index region is surrounded by a low refractive index medium.

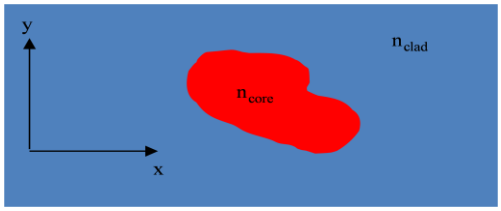

Figure.5 Illustration of a cross section of a general waveguide that consists of a region with high refractive index surrounded by a low refractive index medium.

Assuming a wave propagating in the z direction ($E = E(x,y)e^{j(\omega t-\beta z)}$) and substituting the solution in the wave equation (eq.10), we obtain:

$$\frac{\partial^2 E(x,y)}{\partial x^2}+\frac{\partial^2 E(x,y)}{\partial y^2}+\left(k^2 n^2(x,y)-\beta^2\right)E(x,y)=0$$

This is an eigenvalue problem where the electric field is the eigenvector and the propagation constant is the eigenvalue. There are many modes that solve this problem but not all of them are guided modes. In order for a mode to be guided we expect the evanescent field to decay exponentially so that

$$\left(k^2 n_{clad}^2-\beta^2\right)<0 \quad (46.)$$

If the electric field decays exponentially in the transverse direction, it should have the maximum amplitude inside the core, the electric field at the maximum point should satisfy the condition

$$\left(\frac{\partial^2 E(x,y)}{\partial x^2}+\frac{\partial^2 E(x,y)}{\partial y^2}\right)_{E=E_{max}}<0$$

$$\left(k^2 n_{core}^2-\beta^2\right)>0 \quad (47.)$$

As a result, we will have an oscillatory wave in the core and a decaying wave in the clad. There are also solutions that radiate to the clad, and in such a case the above conditions (eq.46-47) do not apply.

2.2.3 SOI Waveguide

As previously mentioned, Silicon On Insulator is used in certain CMOS processes. Besides the advantage of being compatible with microelectronics, SOI has another great advantage in the context of photonics, namely the high refractive index of silicon. Silicon has a refractive index of 3.46, whereas silicon oxide

has a much lower refractive index of 1.46. This large index contrast results in a critical angle (eq.26) of 25 degrees for silicon –silicon oxide interface. Silicon Nitride has a refractive index of 1.98 which results in a critical angle of 40 degrees for silicon nitride –silicon oxide interface. Equation 33 shows us that for a given mode m the smaller the waveguide width (d), the smaller the angle needs to be. Therefore, high index contrast is advantageous because it supports such small angles, due to the fact that its critical angle is small. This however, does not apply for the fundamental (m=0) mode. For the fundamental mode there is no cutoff for a symmetric slab. Yet, better mode confinement is achieved with large index contrast. Thus, the high refractive index of silicon and silicon nitride allow us to build submicron waveguides. For comparison, the critical angle in a standard optical fiber is $80^0$and it has a core diameter of 9 microns.

2.3 Surface Plasmon Polaritons

Metallic medium can be described as a dense liquid of free electrons. As such it has vibrations which are named plasmons. In this section we will explain Surface Plasmons Polaritons (SPP), which are oscillations of electrons coupled to an electromagnetic wave and propagating on the surface of the metal. In order to examine the SPP we first need to deduce the dielectric function of metals.

2.3.1 The dielectric function of free electron gas

The dielectric function of free electron gas can be described by the Drude model [42]. The motion of an electron oscillating in a sea of electrons under an external force originated from an electric field E can be explained using a simple motion equation:

48. $m\ddot{x} + m\gamma\dot{x} = -eE$

If we assume the field is in the form of $E = E_0 e^{-i\omega t}$ a solution to this equation will be $x = x_0 e^{-i\omega t}$ which gives that:

49. $x(t) = \frac{e}{m(\omega^2 + i\gamma\omega)} E(t)$

Using the definitions for polarization $P = -nex$ and displacement field $D = \varepsilon_0 E + P$ one obtains:

50. $D = \varepsilon_0 \left(1 - \frac{\omega_p^2}{\omega^2 + i\gamma\omega}\right) E$

$\omega_p^2 = \frac{ne^2}{\varepsilon_0 m}$ is the plasma frequency of the free electron gas. The term in the parenthesis is the dielectric function of the metal:

$$\varepsilon(\omega) = 1 - \frac{\omega_p^2}{\omega^2 + i\gamma\omega} \quad (51.)$$

One may observe that this is a complex function so that $\varepsilon(\omega) = \varepsilon_1(\omega) + i\varepsilon_2(\omega)$.

2.3.2 Surface Plasmon polaritons at a single interface

We examine the feasibility of a metal-dielectric interface to support surface waves, by solving the mode equation for TM. From eq.42 we obtain:

$$e^{k_{xi}(d_i)}\left(1 + \frac{\varepsilon_{i+1}}{\varepsilon_i}\frac{k_{xi}}{k_{xi+1}}\right) = 0$$

$$\frac{k_{xi}}{k_{xi+1}} = -\frac{\varepsilon_i}{\varepsilon_{i+1}} \quad (52.)$$

From eq.38 and eq.52 we can deduce the dispersion relation of SPP propagating between two slabs:

$$\beta = k_0\sqrt{\frac{\varepsilon_i\varepsilon_{i+1}}{\varepsilon_i + \varepsilon_{i+1}}} \quad (53.)$$

From eq.52 we deduce that if $\varepsilon_i > 0$ and $\mathrm{Re}(\varepsilon_{i+1}) < 0$ surface waves at TM polarization are supported by the interface. The combination of $\varepsilon_i > 0$ and $\mathrm{Re}(\varepsilon_{i+1}) < 0$ at optical frequencies typically implies metal insulator interface.

Similarly, we can check is such surface waves are supported by the interface also in TE polarization, by trying to solve the mode equation for TE. from eq.40 on obtains

$$e^{k_{xi}(d_i)}\left(\frac{k_{xi}}{k_{xi+1}} + 1\right) = 0 \Rightarrow k_{xi} + k_{xi+1} = 0$$

Since exponential decay requires $\mathrm{Re}(k_{xi}), \mathrm{Re}(k_{xi+1}) > 0$ the only solution for TE polarization is the trivial solution of zero amplitude, so TE polarized surface waves are not supported by this single interface geometry.

2.3.3 IMI

After considering the simple case of a single interface, we now examine the structure of a metal slab sandwiched between two dielectrics materials. If the middle slab width, d, is very large eq.43 reduced to:

$$\varepsilon_i\varepsilon_{i+1}k_{xi+1}k_{xi+2}+\varepsilon_{i+1}k_{xi}k_{xi+2}\varepsilon_{i+1}+\varepsilon_{i+2}k_{xi+1}\varepsilon_i k_{xi+1}+\varepsilon_{i+2}k_{xi}\varepsilon_{i+1}k_{xi+1}=0$$
$$\varepsilon_{i+1}k_{xi+2}\left(\varepsilon_i k_{xi+1}+k_{xi}\varepsilon_{i+1}\right)+k_{xi+1}\varepsilon_{i+2}\left(k_{xi+1}\varepsilon_i+k_{xi}\varepsilon_{i+1}\right)=0$$
$$\left(\varepsilon_i k_{xi+1}+k_{xi}\varepsilon_{i+1}\right)\left(\varepsilon_{i+1}k_{xi+2}+k_{xi+1}\varepsilon_{i+2}\right)=0$$

In order for this last equation to be satisfied, either the first term or the second term must vanish. This indicates the possibility of supporting two separated surface plasmon modes, localized on the surface between the metal and the dielectric. Numerical solution of eq.43allows to extract the effective refractive index of the modes. The mode equation can be simplified by assuming symmetric structure, i.e. the same dielectric material from both sides of the metallic layer. In such a case, on goes back to eq.44. A specific interest is that of a thin metallic slab. For such a case, the two plasmonic modes are coupled. An example for such a case is shown schematically in Figure.6, where a thin (20 nm) aluminum slab is sandwiched between two silicon oxide slabs

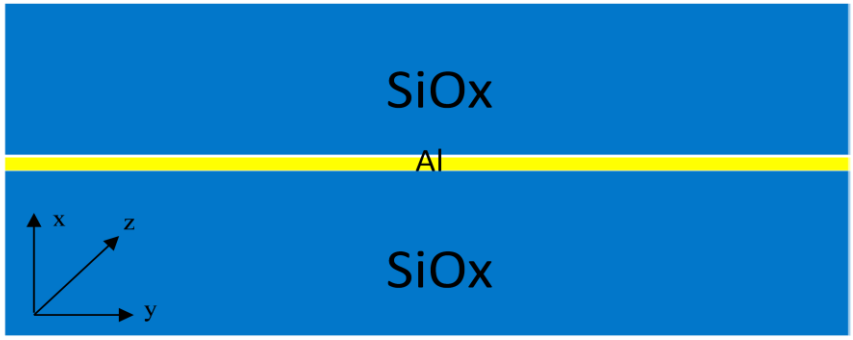

Figure.6 Illustration of an IMI structure with S_iO_x as the dielectric material and aluminum as the metal.

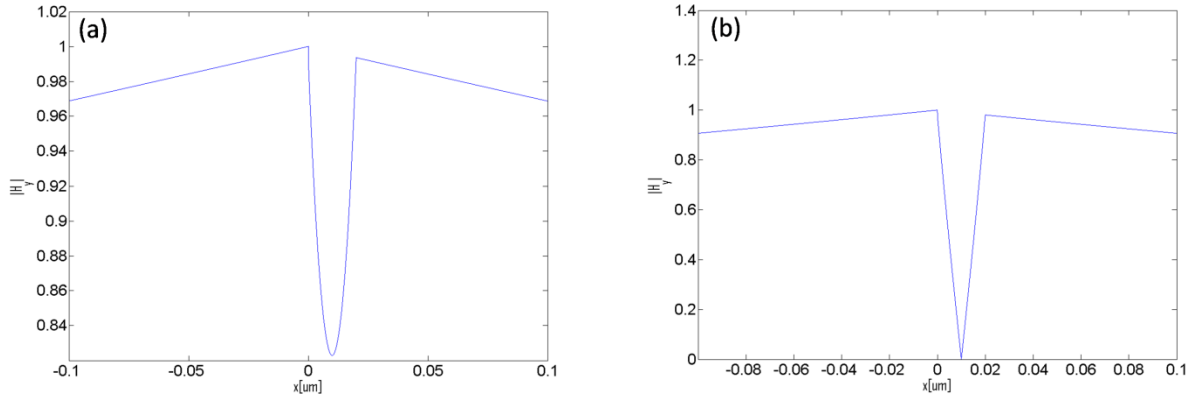

Figure.7 The absolute value of the Magnetic field distribution along the x axis for an IMI structure. a) Symmetrical solution (low losses), (b) anti-symmetrical solution (high losses).

2.3.4 Long Range SPP

For the case of a thin metallic slab, we obtain two modes, one with losses ($n_{eff} = 1.472 + i \cdot 1 \cdot 10^{-4}$), known as the Long Range SPP [43], and has an effective refractive index similar to the oxide, and another mode having the real part of its refractive index closer to that of the metal and its losses are higher. Ohmic losses can be explained as currents, and as such they are proportional to $J \cdot E$. Currents are the result of the electric field in the propagation direction (z) which is proportional to the derivation of H_y in x. In Figure.7.a we present a symmetrical solution which results in close to zero E_z on the metal and a mode with low losses. We focused on this long range SPP. Specifically, we explore the properties of this mode when the symmetry is broken, e.g. by replacing one of the oxide dielectric slabs with a new dielectric slab consists of Si_3N_4.

We now replace one of the oxide slabs withSi_3N_4 and re-solve the mode equation (43). Again, two modes are obtained, but both of them exhibit higher losses compare with the mode in the symmetric case ($n_{eff} = 1.482 + i \cdot 1 \cdot 10^{-3}$ and $n_{eff} = 2 + i \cdot 1 \cdot 10^{-2}$). In order to achieve a mode with lower losses we can add additional slabs with different refractive indexes in order to generate a more symmetric-like dielectric environment and a result to improve the symmetry of the mode. We consider the case of six slabs consisting of: oxide-silicon-thermal oxide-Al-nitride-air(Figure.8) for different width of thermal oxide (tox).We assume that the Al is sandwiched between a 500nm Si_3N_4slab and a 340nm oxidized silicon slab which in turn is placed on an infinite oxide slab (a structure similar to our device). We gradually change tox from 0.29μm to 0.34μm and the silicon slab from 0.195μm to 0.17μm respectively. The ratio between the change in tox and the thickness of the silicon is determined by the physical process of oxidation, the

stoichiometric ratios and volume densities of silicon and silicon dioxide. Specifically, an addition of 2 nm of oxide consumes about 1 nm of silicon. For each of these cases we solve the mode equation with Matlab by using the algorithm showed in eq.40.

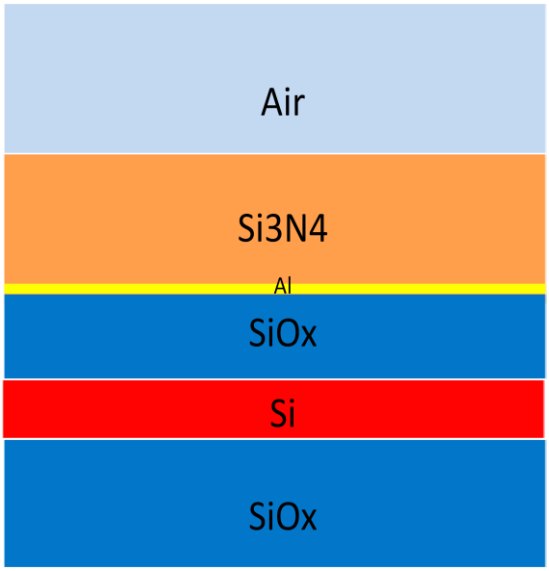

Figure.8 Illustration of a multiple slab IMI structure with an infinite slabs S_iO_x, silicon slab, S_iO_x slab, Al slab, S_iN_4 slab and air

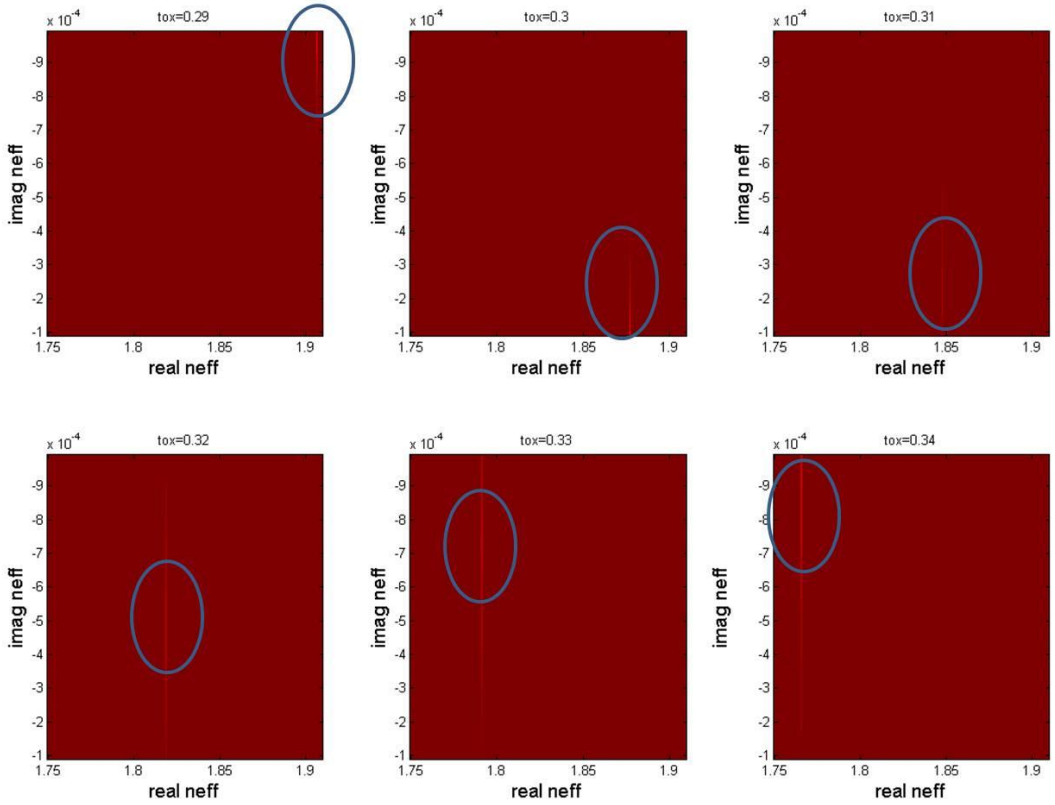

Figure.9 The LR-SPP mode solution for an ox-Si-tox-Al-Ni-air structure for different tox width as function of the real and imaginary effective refractive index. The image is the absolute value of the mode equation and the solution is obtained when the value is zero.

We can see in Figure.9 that changing the dimensions of the slab can result in a mode that will propagate longer (lower imaginary neff) and we can see that there is an optimum solution at 300nm implying symmetry around that point.

2.4 Loss mechanisms in waveguides

One of the goals when we design and manufacture a waveguide is to minimize the losses. There are three major loss mechanisms for light propagating within a waveguide:

2.4.1 Scattering loss

When we design a waveguide we assume smooth walls. In practice, this is never the case, and some roughness is always present. In the presence of roughness one should look on the reflection from the

interface of the core and the clad differently compare with the standard analysis of specular reflection, as shown in Figure.10

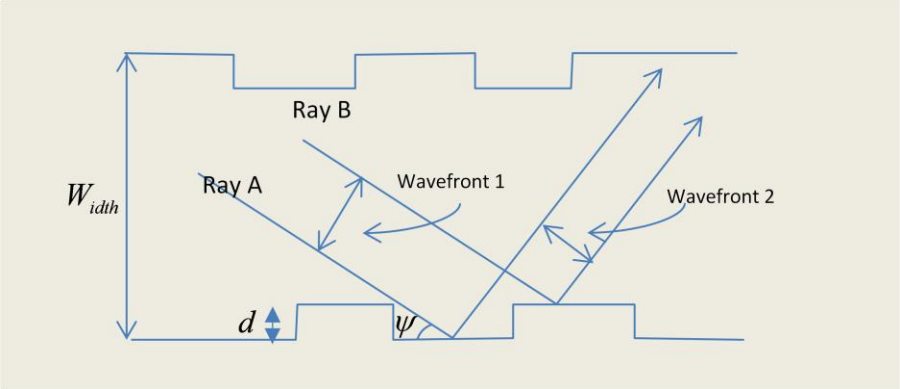

Figure.10 Reflection from a graded interface of two rays.

This means that even at total internal reflection the power returning from the surface according to the Rayleigh criterion [44] will be:

$$\underline{54.}\quad P_r = P_i e^{-\left(\frac{4\pi d}{\lambda}\sin\psi\right)^2}$$

$$P_t = P_i\left(1-e^{-\left(\frac{4\pi d}{\lambda}\sin\psi\right)^2}\right) \approx E^2 \sin\psi\left(\frac{4\pi d}{\lambda}\sin\psi\right)^2$$

The power flow of the mode is

$$I \approx E^2 \cos\psi \cdot W_{idth}$$

This will result in attenuation of light propagating within the slab waveguide:

$$\alpha = \left(\frac{4\pi d}{\lambda}\right)^2\left(\frac{\sin^3\psi}{\cos\psi}\right)\frac{1}{W_{idth}}$$

This calculation does not take in to account the density of the grating but it shows us that the losses are larger for higher modes (bigger angle) and smaller waveguides.

2.4.2 Absorption losses

There are three types of absorption loss that are relevant to our waveguide. The first, free carrier absorption, was discussed in the dielectric function of electron gas (2.3.1) and SPP. The second is interband absorption. If a photon has sufficient energy to transfer an electron from the valance to the conduction band it can be absorbed by the material. Silicon has a gap of 1.12ev and the standard wavelength of optical communication (1550nm) is 0.8ev, so the linear absorption loss in silicon is negligible. The third absorption mechanisms comes from the Si-H bond .In the deposition process of Si_3N_4 imperfections of Si-H bond are created. These bonds have a vibration level at 4650nm. The vibration level third harmonic is 1550nm which is our operating wavelength and it have been shown that Si_3N_4 waveguides can suffer from losses due to bond absorption [45, 46]

2.4.3 Radiation losses

In a bended waveguide the wave front inside the waveguide needs to move as fast as the wave front at the side of the waveguide, both wave fronts need to have the same angular phase velocity:

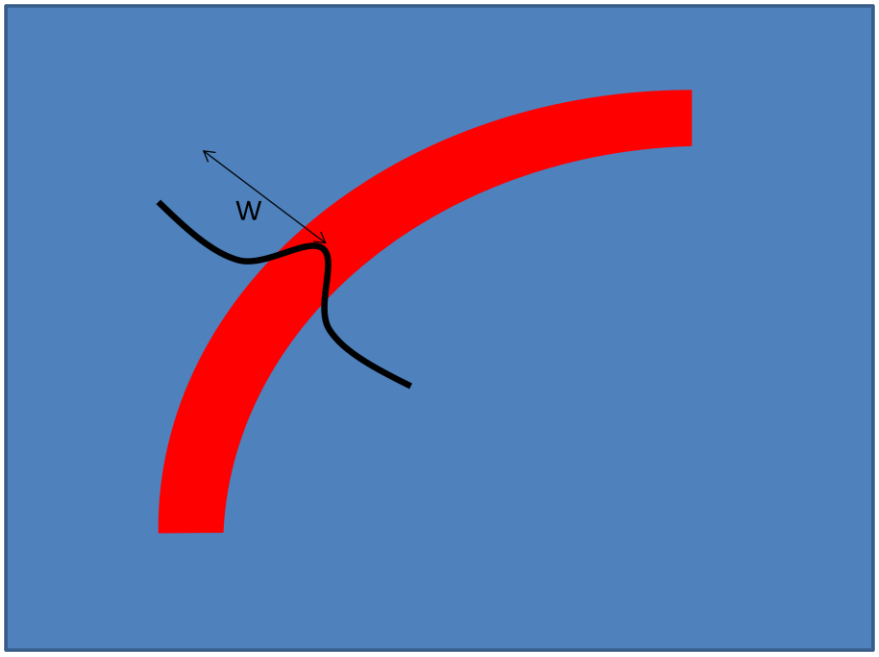

Figure.11 Illustration of Waveguide bending and the electric field that propagate in the waveguide

55. $$\beta_{clad}(R+W)\frac{d\theta}{dt} = \beta_{core}(R)\frac{d\theta}{dt} \Rightarrow R = \frac{W\beta_{core}}{\beta_{core}-\beta_{clad}}$$

If eq.55 is not held light will radiate away from the waveguide to the clad. In order to fabricate dense devices it is necessary that we will be able to fabricate bended waveguides, eq.55 shows us that a waveguide with high index contrast and confined modes can have sharp bends.

2.5 Finite Element Method

While analytic solutions of the wave equation can be found for slab waveguides and other 1-D layered structures, this is not the case for the general 2-D case. Solutions can be found either using approximations or by applying numerical solutions. In order to calculate the mode in our waveguide we used Finite element method [47] simulation. In finite element method we divide our waveguide into a grid of triangular elements (Figure.12.a).

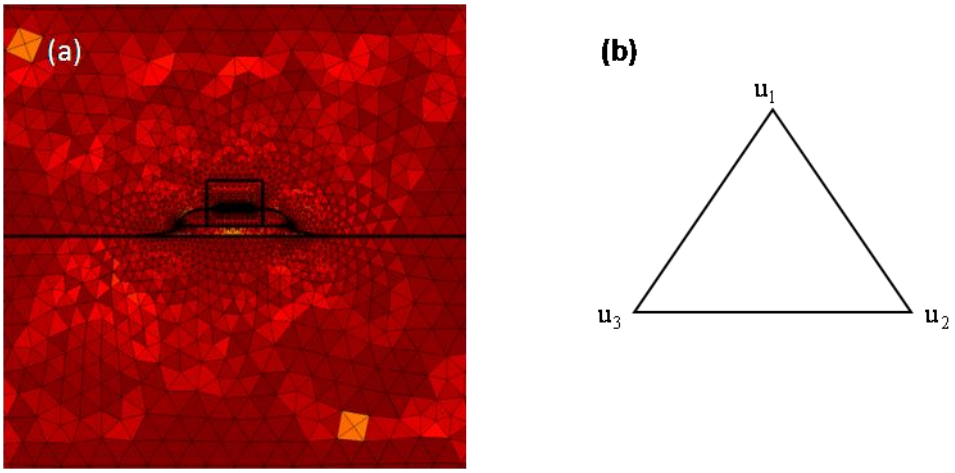

Figure.12 a) Mesh of the waveguide as it calculated by Comsol, b) computational unit of the mesh.

For each triangle (Figure.12.b) were present the field as the sum the field in its vertexes.

$$E(x,y)=\sum_{1}^{3} u_i N_i(x,y)$$

$$N_i(x,y)=a_i x+b_i y+c_i$$

Instead of solving the wave equation, the simulation solves a variational problem that can be represented in a matrix form.

$$\vec{\nabla}\times(\vec{\nabla}\times\vec{E})-\varepsilon\mu_0\omega^2\vec{E}=\vec{d}\Rightarrow\begin{bmatrix}K_{11} & K_{12} & K_{13}\\ K_{21} & K_{22} & K_{23}\\ K_{31} & K_{32} & K_{33}\end{bmatrix}\begin{bmatrix}u_1\\ u_2\\ u_3\end{bmatrix}=\begin{bmatrix}d_1\\ d_2\\ d_3\end{bmatrix}$$

We get a matrix that represents the field in that triangle. Assembling all the matrix elements into one global matrix generates an eigenvalue problem and its solution allows us to find the electric field and effective index of each mode.

$$[E]=K^{-1}d$$

2.6 NSOM measurements

NSOM stands for Near field Scanning Optical Microscope. Near field Microscope detects EM fields from a distance which is less than a wavelength from the source. Its major advantage is resolution. Being based on near field imaging it can detect light with resolution much better than the diffraction limit. Consider an object of limited size with transmittance of $f(x,y,0)$. Its spatial frequency spectrum $F(u,v)$ can be written as [48]:

56. $$F(u,v)=\int_{-\infty}^{\infty}\int_{-\infty}^{\infty}f(x,y,0)e^{-j2\pi(ux+vy)}dxdy$$

This spectrum is a collection of plane waves. At plane z each plane wave accumulates a phase term and thus it can be written as:

57. $$F(u,v,z)=F(u,v)e^{jk\sqrt{1-u^2\lambda^2-v^2\lambda^2}}$$

For high spatial frequencies we obtain $\left[1-u^2\lambda^2-v^2\lambda^2\right]<0$ and thus these frequency components decay as they propagate so when we look at sources from the far field we lose resolution. Yet, if we look from close range we can still capture the higher frequencies and as a result higher resolution beyond the diffraction limit is obtained. In order to exploit this possibility we need a very small detector in close proximity to the sample. Our NSOM plays the role of this detector. Essentially, our NSOM is an Atomic Force Microscope, it which that standard AFM probe is replace by a pulled fiber which is coated with metal except for a small opening at the apex of the probe. The evanescent waves are coupled into the

probe and are able to be transmitted through its100-300nm aperture. These waves continue to propagate in the fiber (Figure.13) towards a photodetector. The tip is scanning the sample using a piezo stage and generates up to 30x30 μm^2 images.

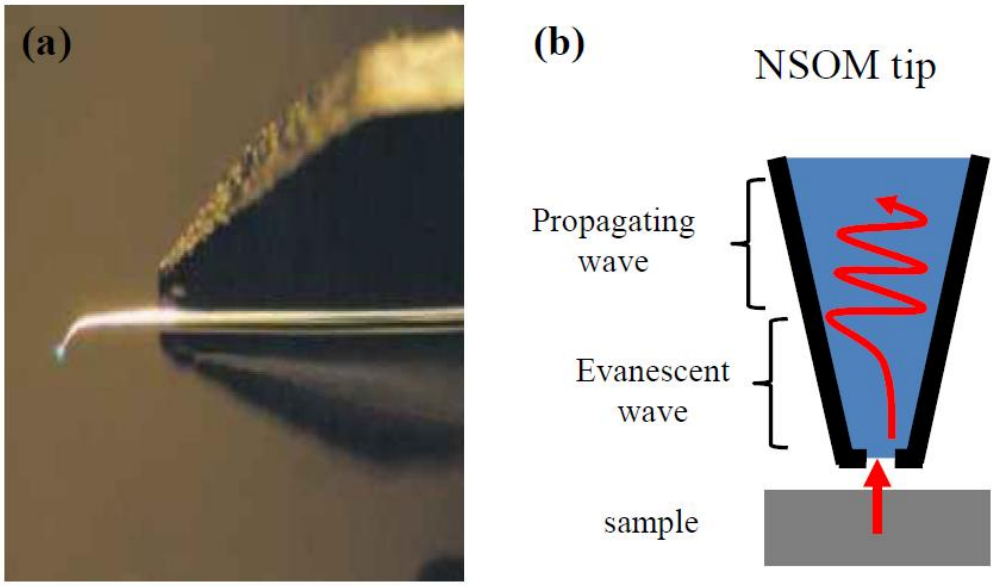

Figure.13 a) NSOM tip, b) NSOM operating scheme

2.7 Coupling of light between waveguide and a lensed fiber

Once a waveguide is ready, one needs to characterize its properties by launching light from an external fiber into the waveguide and by collecting the light emendated from the waveguide into another fiber. Calculating the power transmission from one mode in a waveguide to another mode in can be done using the overlap integral between the two modes.

$$\eta = \frac{\left|\int E_1 E_2^* dxdy\right|^2}{\int |E_1|^2 dxdy \int |E_2|^2 dxdy} \quad (58.)$$

In the case of silicon photonics most of the waveguides dimensions are sub micron, but the standard single mode fiber has a diameter of 9um which results in a mode overlap of less than 1%. Standard solution for increasing the coupling efficiency is by using lensed fibers.

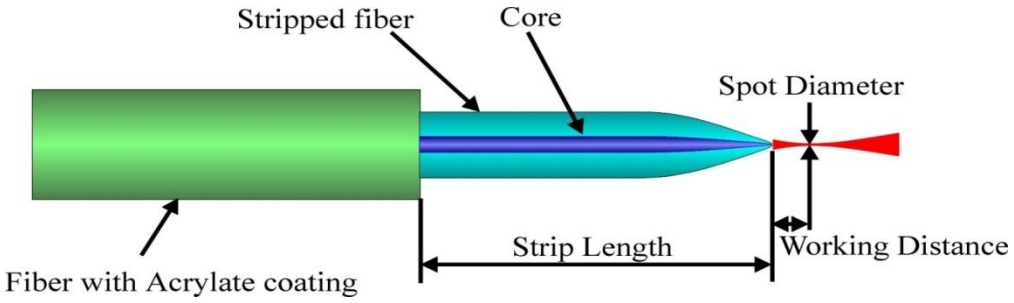

Figure.14 Illustration of a Lensed fiber

The lensed fiber (Figure.14) is manufactured by polishing the end face of the fiber to a specific radius and taper angle, forming a lens. The lensed fiber confines the beam to a 2.5um spot diameter, still larger than the cross section of our device. In order to get better matching one can use an adiabatic taper (Figure.15) at the end of the waveguide.

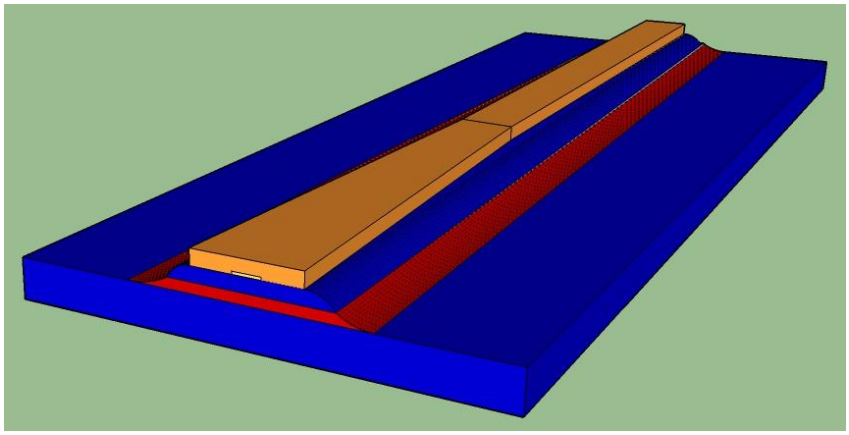

Figure.15 Illustration of a taper for improvement of the coupling between the lensed fiber and the waveguide.

The slow gradient change in the taper maintains high overlap between the modes and results in better coupling.

2.8 Signal improvement

Detecting a high quality NSOM signal can be difficult in cases of small signal and high noise. To overcome this challenge we have used the following two approaches.

2.8.1 Erbium doped fiber amplifier

An erbium doped fiber amplifier (EDFA) is used to amplify the signal around 1550 nm wavelength. The basic operation of erbium doped fiber is explained in Figure.16

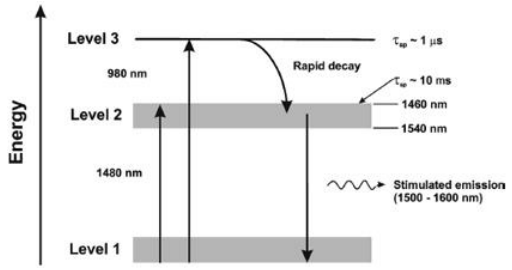

Figure.16 Erbium amplification scheme

A 980 nm laser excites the erbium ions from level 1 to level 3 where they rapidly decay to level 2. A 1550nm photon that is interacting with an ion in level 2 will cause the ion to drop to level 1 while emitting a 1550nm photon.

2.8.2 Lock in amplifier

Another approach to increase the signal to noise ratio of the measurement is by using a lock in amplifier. This device filters out most of the noise by modulating the signal at a specific frequency and performing detection at this frequency only. In order to use the lock in amplifier we first need to modulate our signal. The modulated output, V_{sig}, is then multiplied with a reference modulated signal, V_L, resulting in:

59. $$V = V_{sig} V_L \sin\left(\omega_r t + \theta_{sig}\right)\sin\left(\omega_L + \theta_{ref}\right)$$

Where ω_r and ω_L are the frequencies of modulation of the signal and the reference signal respectively, θ_{sig} and θ_{ref} are the phases of the signal and the reference signal respectively,

Applying a low pass filter will usually result in nothing, except for the case where $\omega_r = \omega_L$. In such a case, the output of the low pass filter is:

60. $$V_x = \frac{1}{2} V_{sig} V_L \cos\left(\theta_{sig} - \theta_{ref}\right)$$

We receive an amplified signal that reaches a maximum value when the phases of the signal and the reference signal are equal. In our amplifier there is a second detector that detects with a ref of 90^o offset resulting in a second output of $V_y = \frac{1}{2} V_{sig} V_L \sin\left(\theta_{sig} - \theta_{ref}\right)$ and a total output of:

61. $V_R = \sqrt{V_x^2 + V_y^2} = \frac{1}{2} V_{sig} V_L$

Our final output has no dependence on the reference phase.

3. Proposal :LR-DLSPPW

In this chapter I will explain our device design concept and present the simulations we preformed in order to deduce the device sensitivity to fabrication errors and its modal content.

3.1 Device explanation

Our first goal was to design a CMOS compatible LR-DLSPPW. SOI is used in certain CMOS process and is compatible with our need for a low index box with higher dielectric material above it in order to achieve mode confinement. Our selection for ridge material is Si_3N_4 that can be deposited by PECVD with high quality. Unfortunately silicon and Silicon Nitride have refractive indexes of 3.47 and 1.98 respectively, and thus cannot be used for creating a symmetric dielectric environment with respect to the metal between them, as required for the long range SPP. The solution to this problem is achieved by partially oxidizing the silicon, creating a thermally grown silicon oxide layer on top of it. The parameters of the oxide-silicone-oxide layer stack can be tuned to create effective refractive index which is similar to that of the silicon nitride and by doing so to generate a symmetric-like environment for the metal. The basic LR-DLSPPW as it was proposed in [30] is presented in Figure.17.

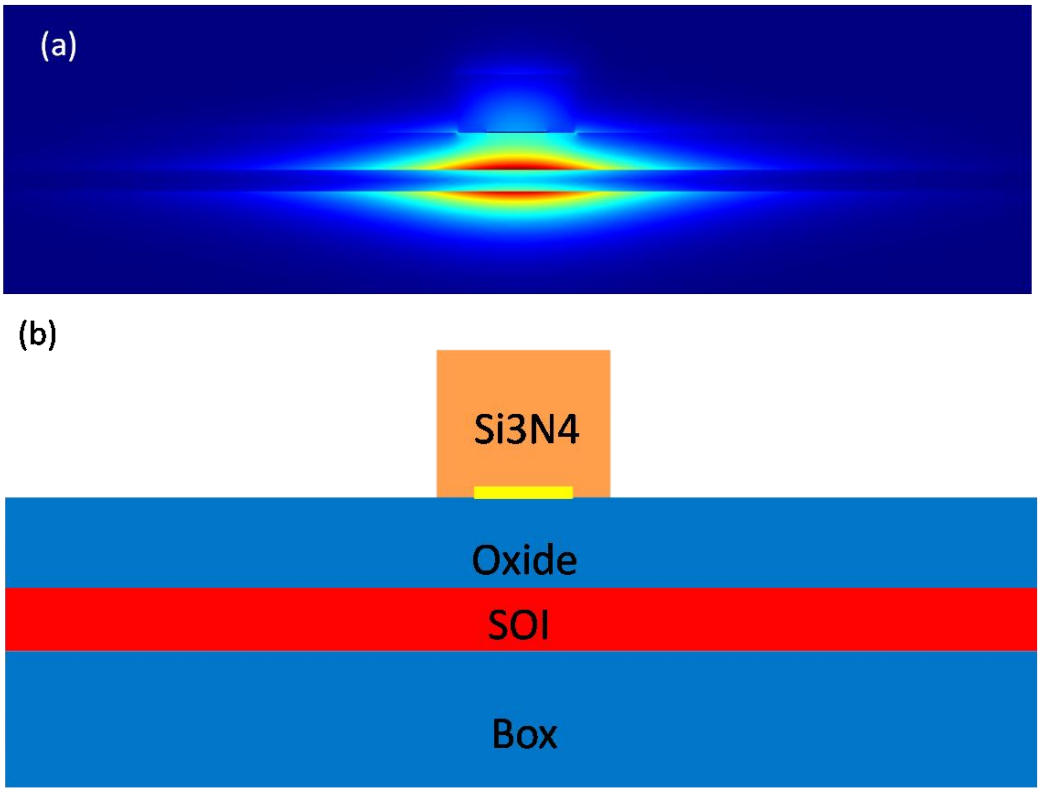

Figure.17 a) Electromagnetic simulation showing the intensity profile of the modes in the "old" LR-DLSPPW (b) Schematic cross section of the device

Due to the high refractive index of silicon the mode expands to the silicon slab waveguide. In order to achieve higher confinement we need to etch through the silicon. Our device mostly support the mode presented in Figure.18

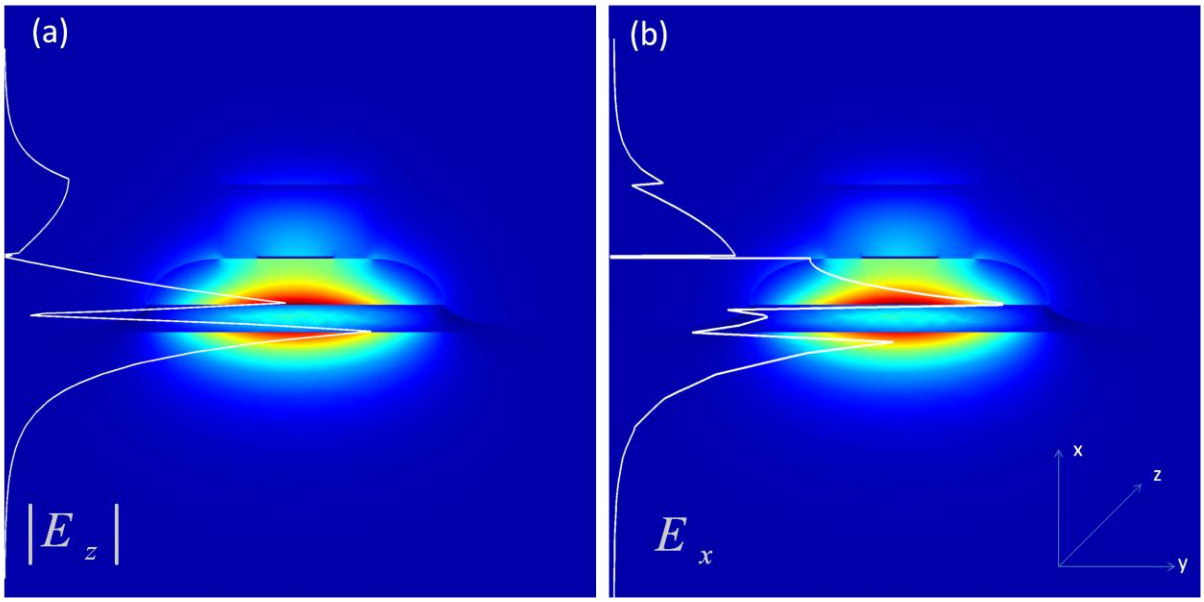

Figure.18 a) Electromagnetic simulation showing the intensity profile of the mode and the absolute value of the electric field in the propagation direction at a cross section taken in the middle of the waveguide. b) Electromagnetic simulation showing the intensity profile of the mode and the absolute value of the electric field perpendicular to the metal strip at a cross section taken in the middle of the waveguide.

We can notice certain symmetry of E_x around the metal that result in minimum point for E_z on the metal and low loss mode.

3.2 Simulations

3.2.1 Device sensitivity

Our LR-DLSPPW (Figure.19) consists of Si3N4 ridge deposited on top of a thin aluminum strip which is supported by an oxidized SOI wafer. The Si3N4 and SiO2 width were determined in an effort to create a symmetric-like environment, in which, a LR-SPP mode will develop with minimal ohmic losses. Using Finite Element Mode solver (FEM) we calculated the propagation length of the fundamental mode as a function of various design parameters. These simulations are essential for the purpose of determining the device parameters as well as for estimating the sensitivity to unavoidable deviation that occurs in the fabrication process. The simulation results are plotted in Figure.20. As a starting point we have assumed rib height and width of 500 nm and 1 micron, respectively, metal height and width of 15 nm and 500 nm,

respectively, and perfect alignment between the nitride rib and the metal. All calculations were performed based on the real device configuration, shown in Figure.19.b.

As can be seen in Figure.20, propagation length of nearly 2.5 mm is achievable. Furthermore, modifying the rib width and height by few tens of nm has a moderate effect on the propagation length. Misalignment of up to 40 nm between the metal and the rib is still acceptable. The only crucial parameter is the oxide thickness. Indeed, even a slight deviation of ~20 nm in the oxide thickness results in a drastic decrease in the propagation length, towards values of ~1 mm. Nowadays, controlling the oxide thickness within 20 nm accuracy is more than reasonable and thus long propagation length should be possible to be maintained

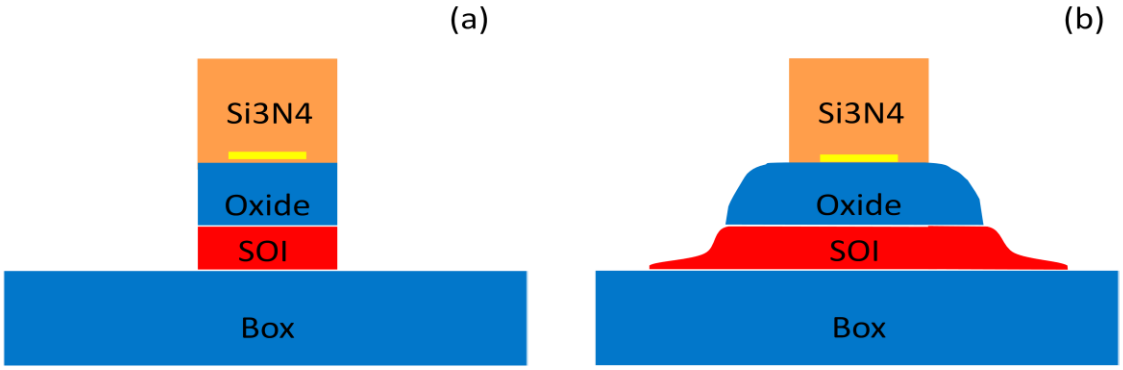

Figure.19 Schematics showing the cross section of an ideal device. (b) Schematics showing the cross section of our fabricated device, taking into account the fabrication constrains.

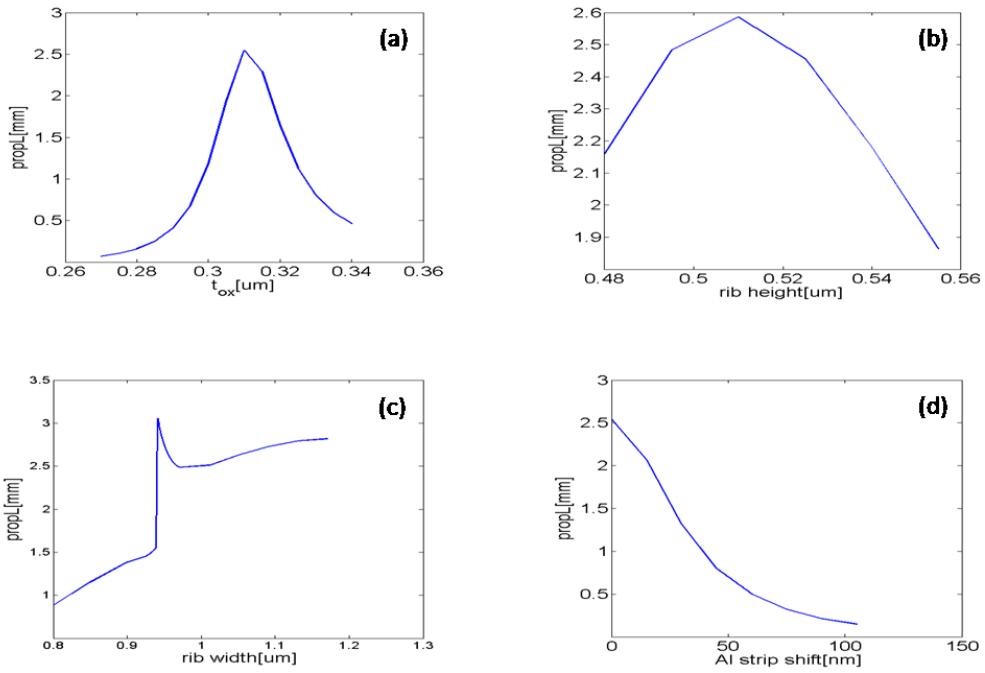

Figure.20 Propagation length dependence in thermal oxide height, b) Propagation length dependence in SiN Rib height, c) Propagation length dependence in SiN Rib width d) Propagation length dependence in Aluminum strip deviation from center.

3.2.2 Supported modes

We calculated the profiles and the properties of the modes that are theoretically supported by the device. Figure.21 shows the 5 modes that are supported by our device at the wavelength of 1550 nm. Yet, by calculating the overlap integral of these modes with a TM polarized Gaussian beam(Figure.22) we came to a conclusion that only the mode which is launched into the waveguide from an external fiber has a non negligible coupling coefficients only to the first and the second modes (Figure.21), and thus only these modes will be excited. According to our simulations the first mode has an effective insex of $1.78+i\cdot 5\cdot 10^{-5}$ and the second has an effective insex of $1.5+i\cdot 8\cdot 10^{-4}$.

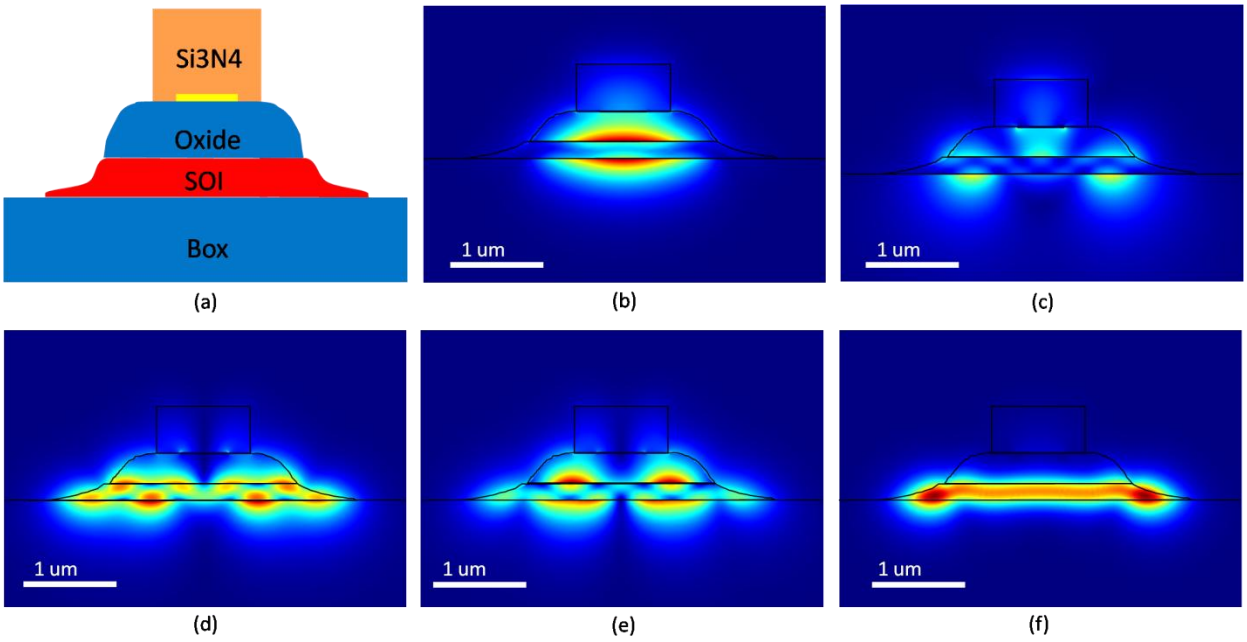

Figure.21 a) Schematic cross section of the device (b,c,d,e,f) Electromagnetic simulation showing the intensity profile of the modes in the LR-DLSPPW

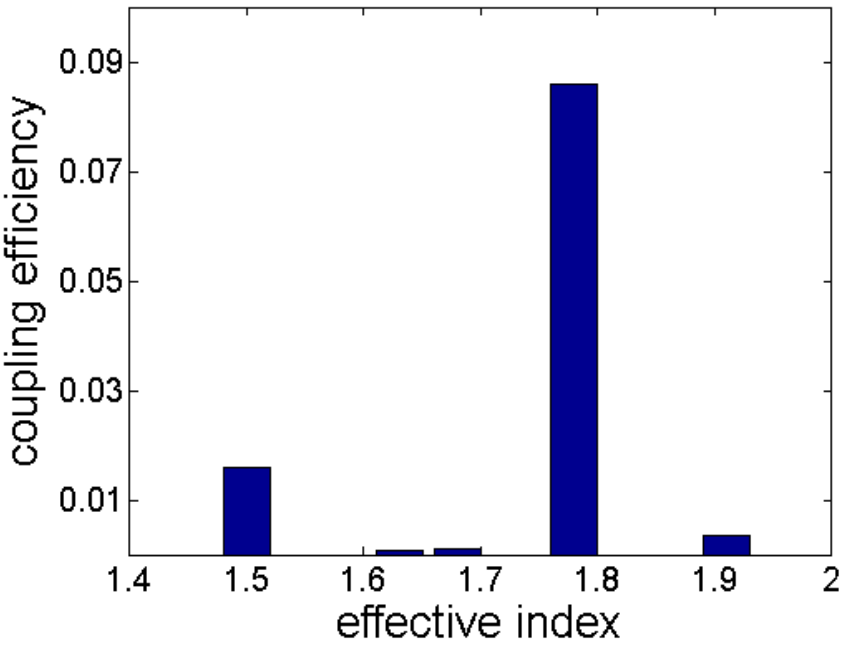

Figure.22 solution to the overlap integral of each mode

4. Fabrication

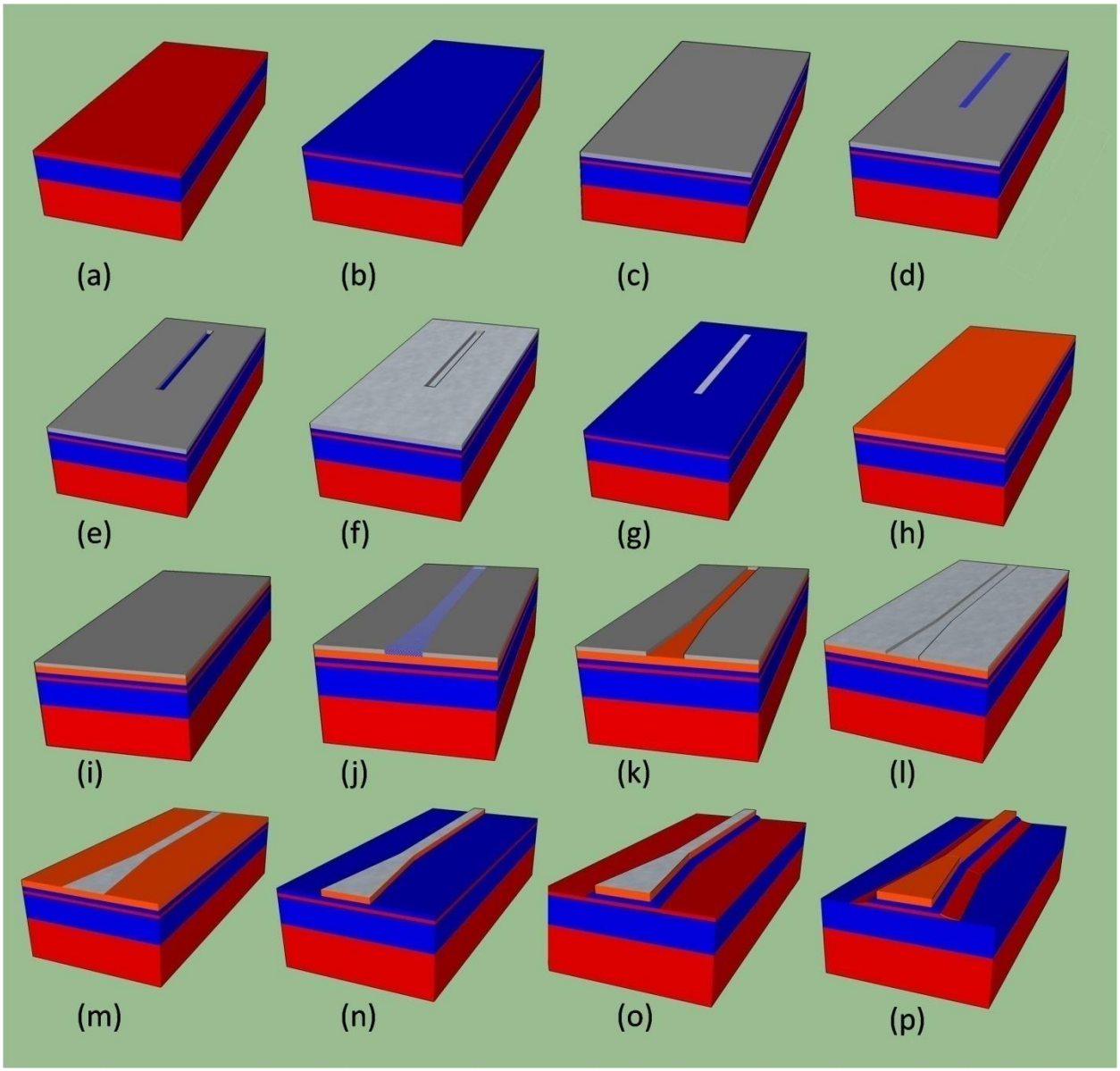

Figure.23 Schematic description of the fabrication process. a) Planar substrate b) oxidation of the SOI; c) resist spun; d) ebeam lithography ; e)development of the resist; f) evaporation of aluminum; g) removal of the resist; h) deposition of Si_3N_4; i)resist spun; j)ebeam lithography ; k) development of the resist; l)evaporation of aluminum; m) removal of the resist; n) RIE of Si_3N_4 ; o) RIE of SiOx; p) RIE of Si

The fabrication process is depicted in Figure.23. We used a SOI (SOITEC) substrate consisting of 340nm-thick crystalline silicon layer on top of a 2μm thick buried oxide (BOX). The BOX functions not only as a lower index cladding but also as a boundary between the waveguide and the lower silicon substrate. If the box is too thin the mode will leak in to silicon substrate. The wafer is sawed in to 2x2 cm chips. The chip is oxidized in a wet process in a furnace at temperature of 920^{o} for 190 minutes, as a result, a 310nm thick silicon oxide layer (SiO_x) was thermally grown. Silicon molecular density is twice the one of SiO_x so 155nm of Si is consumed leaving us with 185 nm of Si. PMMA ebeam resist is spun on the top of the chip and then baked to evaporate the solvent. The patterns are transferred to the resist by using a RAITH ebeam lithography system. The chip is then placed in the evaporator where a 15 nm thick aluminum layer is evaporated on the chip. The sample is placed in front of a crucible holding the aluminum while an ebeam liquidize the metal which is evaporated on the sample. The chip in then washed in N-Methyl-2-pyrrolidone (NMP)at 80^{0}degrees that removes the resist that was not exposed to the electron beam with the metal covering it resulting in a metal strip positioned on the oxidized SOI. This procedure of lithography followed by evaporation and removal of the resist is called "lift off". The chip is then moved into a plasma enhanced chemical vapor deposition (PECVD (Oxford Instruments Plasma lab System 100)) machine where a 500 nm thick Si_3N_4 layer is deposited on it. Deposition is achieved by flowing reactant gases between parallel electrodes, a grounded electrode and an RF-energized electrode.SiH_4 at 20 Standard Cubic Centimeters per Minute (SCCM), NH_3 at 20 SCCM and N_2 at 980 SCCM are flown in to the chamber where the capacitive coupling between the electrodes excites the gases into plasma, which induces a chemical reaction and results in Si_3N_4deposited on the substrate. The substrate, which is placed on the grounded electrode, is heated to 300°C. In comparison, CVD requires much higher temperatures, in the range of 600°C to 800°C, such high temperature cannot be used in our process as it will damage the aluminum strip.

When the Si_3N_4 is deposited at high frequency of 13.6 MHz it is not dense enough consequently creating a tensile stress (Figure.24).When the Si_3N_4 is deposited at low frequency of kHz the ion can react and bombard the sample and create a denser layer consequently creating a compressive stress. The stress can result in cracks in the device and scattering losses. We have used both frequencies in our deposition process. Each cycle was composed of 25 seconds of high frequency deposition and 20 second of low frequency deposition. The second step compensates the stress caused by the previous step for the purpose of achieving a low stress layer.

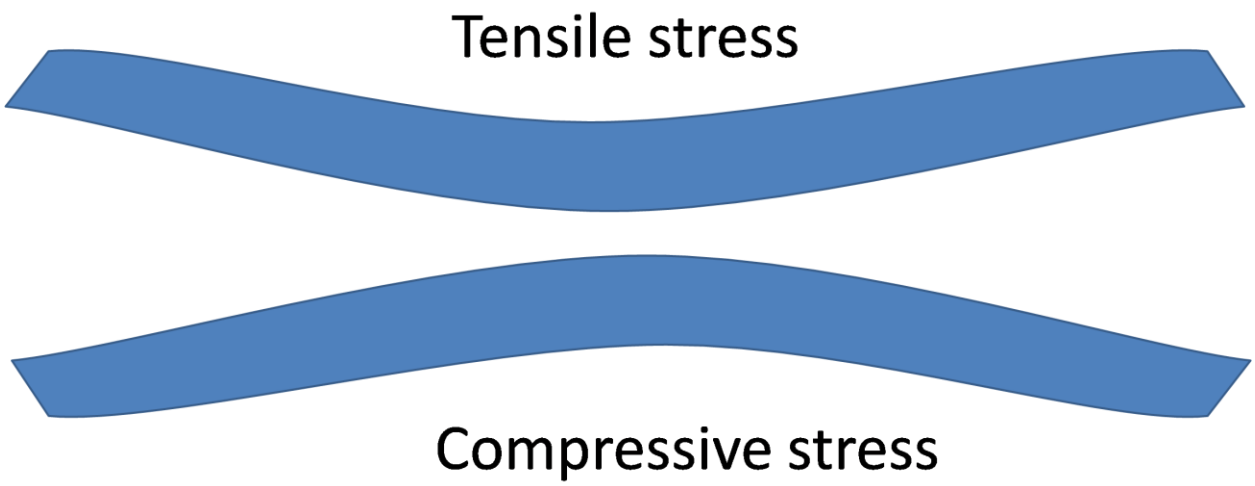

Figure.24 Tensile and compressive stress examples

Next, the metal mask defining the optical structure consisting of the LR-DLSPPW, the input/output photonic waveguides and a 100μm length tapered couplers was patterned using standard lift-off procedure of 120 nm thick aluminum. Finally, we used reactive ion etching (RIE (CORIAL)) to etch the Si_3N_4, SiO_2 and Si. Etching is achieved by introducing reactive gasses to strong RF field. The RF field ionizes the gases creating ions and free electrons. The electron oscillates in the chamber and hit the sample and the sidewalls. Due to absorption of electron, the surface starts to accumulate negative charge, the positive ions then drift to the surface and bombard the sample. The combination of chemical reaction with the sample and the physical bombarding of the sample, at a nearly vertical angle, results in an anisotropic etching. In order to etch the Si3N4 we ionized 100 SCCM of CHF_3, 8 SCCM of O2 and 2 SCCM of He using 170 [watt] RF powers. In order to etch the SiO_2 we ionized 100 SCCM of CHF_3, 4 SCCM of O_2 and 2 SCCM of He using 170 [watt] RF powers. In order to etch the Si we ionized 10 SCCM of CHF_3, 25 SCCM of SF_6 and 5 SCCM of He using 65 [watt] RF powers. To achieve optimal results the device is fabricated in the middle of the chip, and thus we need to cut the chip around the beginning of the tapered waveguide structure. Unfortunately, the sawing procedure may result in a rough facet (Figure.25).

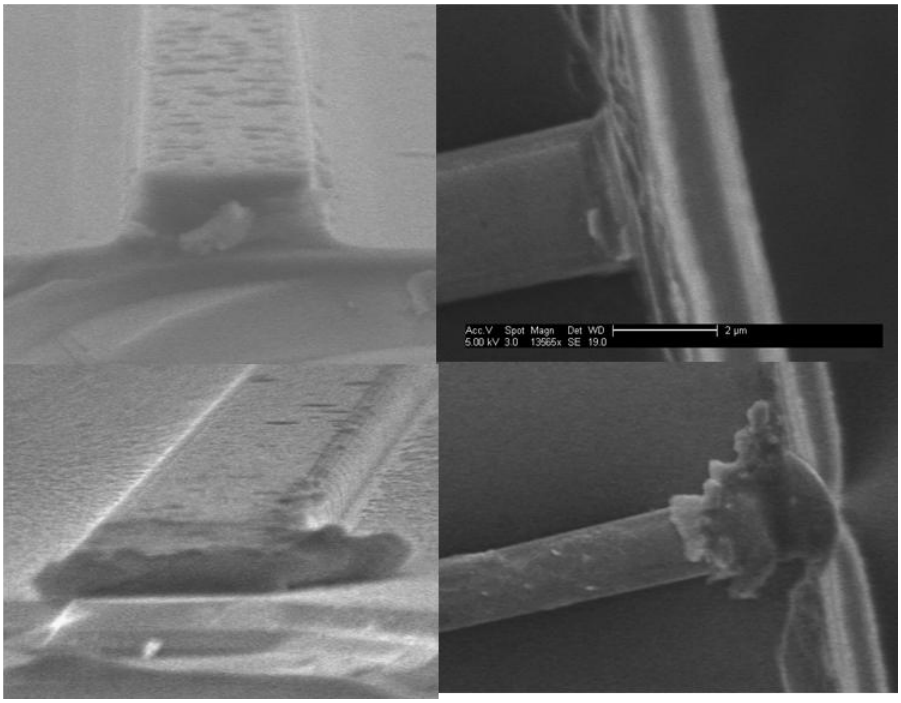

Figure.25 SEM images of the sawed tapers

To verify the quality of the fabrication process we captured a scanning-electron microscope (SEM) image of a typical cross section of LR-DLSPPW prior the metal etching, as shown in Figure.26. One can observe the nice profile of the silicon nitride. Yet, the oxide and the silicon etch should be further optimized.

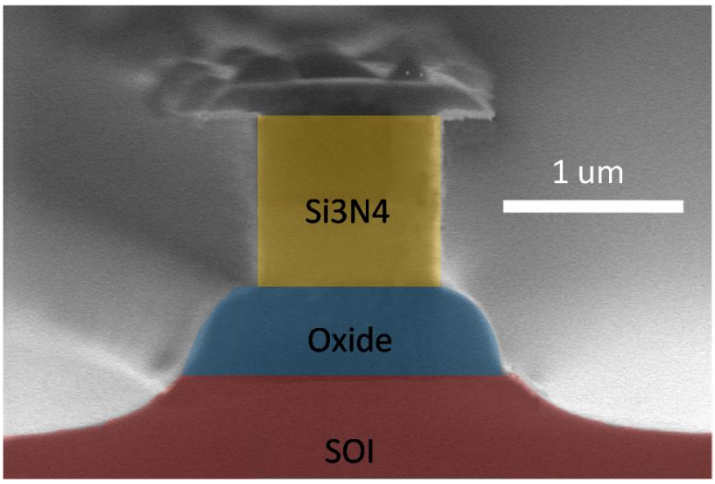

Figure.26 SEM image of the LR-DLSPPW with highlighted different material layers.

5. Measurements

5.1 Measurement setup

In order to measure the device we used the setup that can be seen in Figure.27

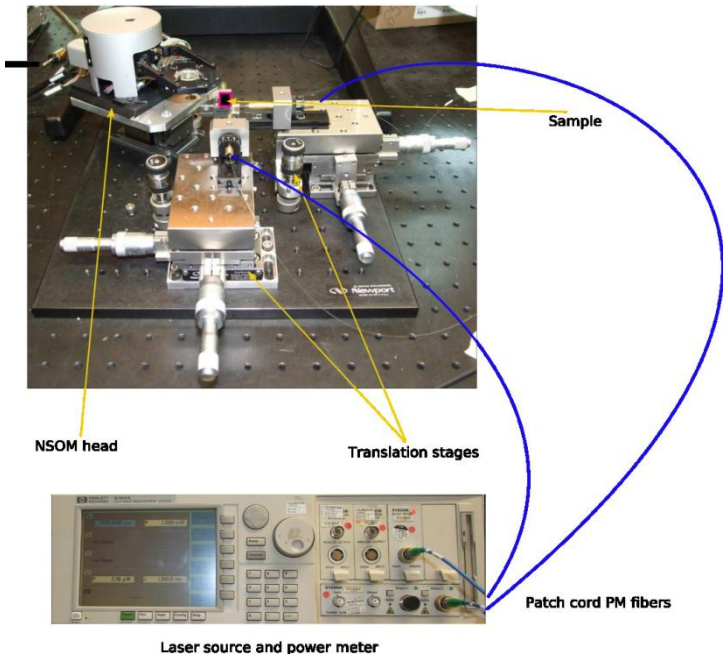

Figure.27 measurement setup

Light generated by a tunable laser (Agilent 81680A), with wavelength range of 1460nm to 1580nm and maximum power of 6dBm, is launched into the waveguides using a polarization maintaining lensed fiber with a mode size of 2.5μm.The light from the output facet of the waveguide was collected with a similar fiber and detected by an InGaAs photodetector (Agilent 81634A), with wavelength range of 800nm to 1650 nm and with power range of 10dBm to -80dBm. The device is mounted on a vacuum chuck holder for mechanical stability. Optimization of the coupling was done using two 3 axes translation stages, which the lensed fibers are placed upon, simply by looking for maximum transmission. After optimum coupling is achieved the NSOM tip is placed on the waveguide and we can start taking NSOM measurements. .Unfortunately, the NSOM signal is typically not strong, especially in this case where the majority of the mode is placed in the oxide, far away from the NSOM

probe. As previously mentioned, in order to enhance the input signal we have used an EDFA and in order to separate our signal from the noise we used a lock in amplifier.

5.2 Loss measurements

To characterize the propagation loss of the device we have fabricated several devices with different lengths, and launched a TM (out of plane) polarized light generated by a diode laser operating in the 1.54-1.56μm wavelength regime. The light was launched into the waveguides using a polarization maintaining lensed fiber with a mode size of 2.5μm. Similarly, light was collected from the output facet of the waveguide by another tapered fiber and detected by an InGaAs photodetector (HP 81634A). To remove the effect of Fabry-Perot oscillations (Figure.28), each measurement was performed by scanning the above mentioned wavelength range and extracting the mean value of transmission. Furthermore, in order to differentiate between inherent absorption losses (occurred in the metal strip) and additional losses that originate from absorption and scattering by the silicon nitride rib waveguide and were neglected in the simulation, we have repeated the same measurement using a reference sample consisting of a similar structure, albeit without the metal layer. The measured transmission results for the two sets of samples are presented in fig.26.We added a 10 dB error bar due to rough and crooked cutting of the tapers.

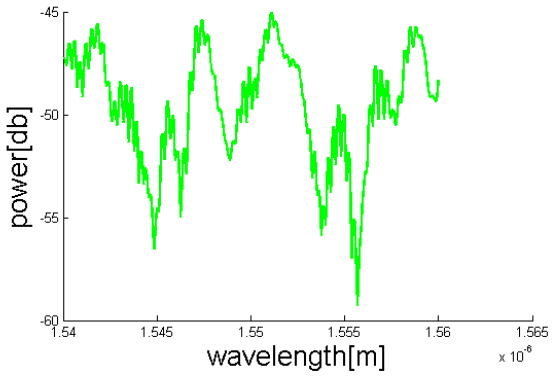

Figure.28 power spectrum of the waveguide

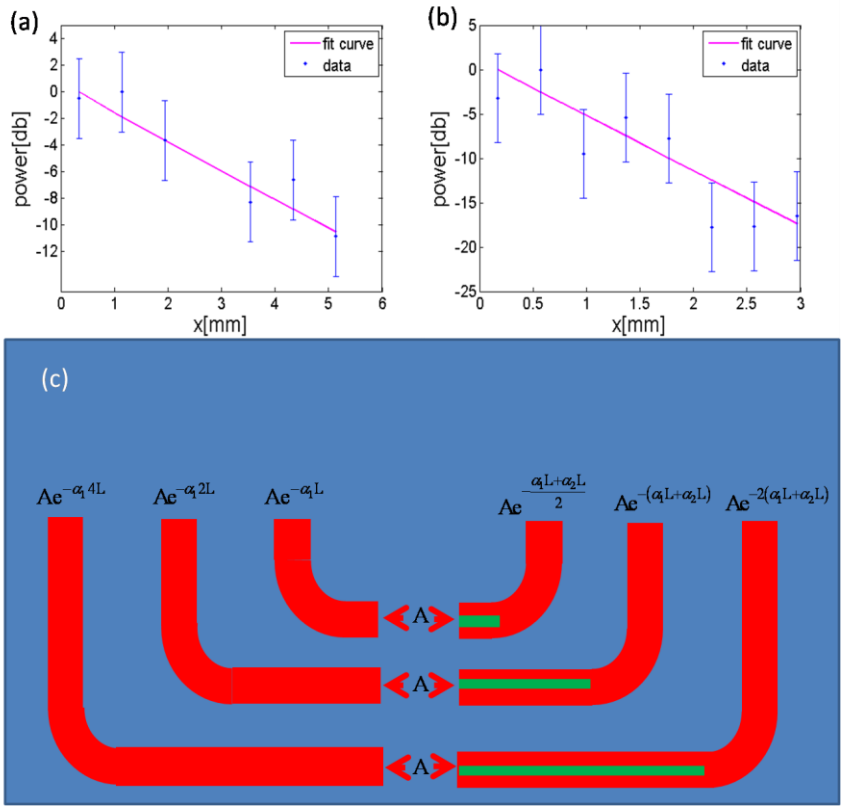

Figure.29 a) input -output ratio for devices with different length without the metal strip, b) Input-output ratio for devices with different length with the metal strip, c) schematic of the measured devices.

Before discussing the loss of the actual plasmonic device, we should consider the loss of the reference sample, i.e., without metal, shown in fig.26 (b). By performing a linear fit to the measured data, we found the propagation loss of this structure to be ~ 2 dB/mm. The reason for the relatively high loss becomes clear by observing the rib surface (Figure.30), in which noticeable surface roughness is evident. We measured the amplitude of the surface roughness to be in the range of 20-40 nm. Indeed, a propagation loss of ~2db/mm is an acceptable number for such values of roughness, as calculated e.g. by Payne and Lacey [49].

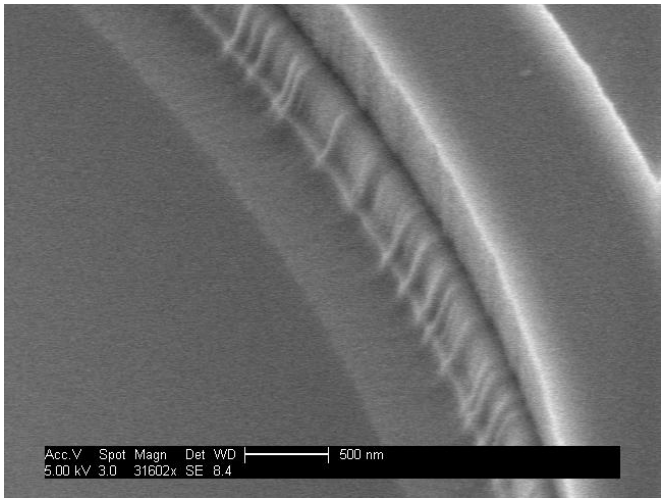

Figure.30 SEM image of the side walls of the LR-DLSPPW

After establishing the origin of propagation loss in the reference sample, we can now analyze the propagation loss in the plasmonic sample. For a given waveguide length 2L, each sample consists of a hybrid plasmonic waveguide of length L which is butt coupled to a reference waveguide of length L. Thus, we first subtract the loss (2 dB/mm) of the reference waveguide. The remaining loss is that of the plasmonic waveguide. This obtained loss is presented in Figure.29 (a) as a function of the waveguide length L. By performing a linear fit to the obtained data the propagation loss of the hybrid plasmonic waveguide was found to be ~6db/mm. Keeping in mind that ~2dB/mm loss is originated from the surface roughness of the dielectric structure, we conclude that the loss originated from the damping in the metal is in the order of 4dB/mm, i.e. corresponding to a propagation length of about 0.7 mm. Comparing to our computer simulations (Figure.20), such a value of propagation length can be explained, e.g. by a ~50 nm misalignment of the Al strip with respect to the nitride ridge. Other reasons can be related to roughness in the Al strip, slight deviation in the thickness of the oxide layer, or combination of all the above. In order to improve the propagation length of the waveguide we should reduce the roughness. The high roughness can be reduced by optimizing the etching process by changing the RF power and gas ratio. The roughness can also be reduced by smoothing the metal mask.

5.3 NSOM measurements

Finally, in order to confirm that our waveguide supports two modes, we performed near-field scanning optical microscopy measurement (NSOM, Nanonics MultiView 4000), in which our metal-coated NSOM probe, with aperture of 250 nm, scanned the top of the hybrid plasmonic waveguide.Figure.31(a) presents a near field optical intensity distribution on top of the silicon nitride (256x256 pixels). The obtained result shows a clear trace of interference between the two modes, as evident by the periodic structure along the propagation direction. The periodicity was measured to be ~5.5 micros, corresponding to a difference of 0.28 in the effective index of the two modes. This is in excellent agreement with the predicted effective index values of 1.78 and 1.5 as can be seen in the mode propagation simulation and the good fit to the NSOM cross section (Figure.31(c)).

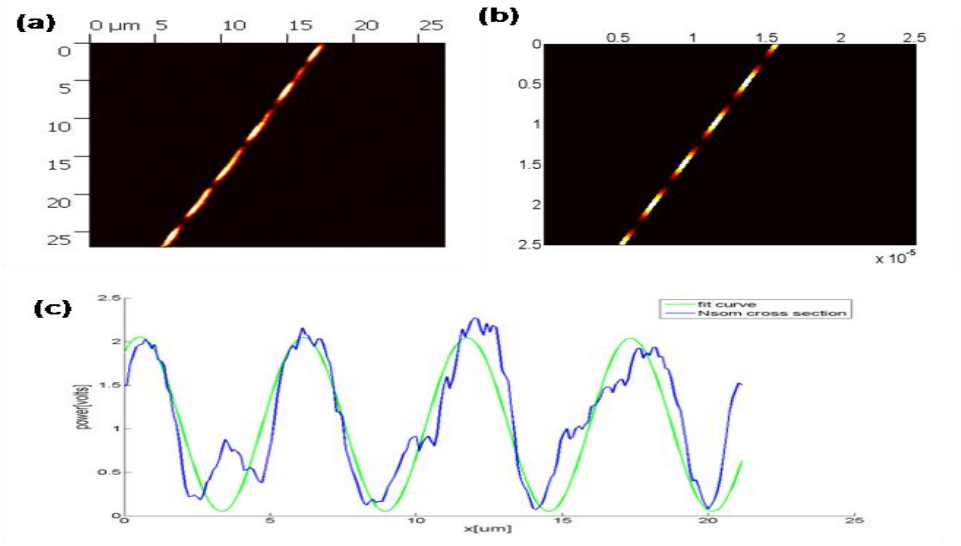

Figure.31 a) NSOM image b) mode propagation simulation c) NSOM cross section

As previously mentioned, the loss of the two modes is very different.According to our simulations the first mode has an effective index of $1.78+i\cdot 5\cdot 10^{-5}$ and the second has an effective index of $1.5+i\cdot 8\cdot 10^{-4}$. As a result,the contrast of the beating decays as the modes propagte along the waveguide.

6. Results Discussion

Our measured device shows losses of ~60dB/cm (~0.7 mm PL). Taking in to account only the ohmic losses we reach a propagation loss of only 40db/cm (~1mm PL). Yet, these value is not as good as the optimum results of 2.5 PL (17dB/cm), predicted by the computer simulations (Figure.20). If we consider the fact that a 15-30 nm misalignment between the metal and the rib can result in 4-15 dB/cm losses and that a 10 nm misalignment in the tox can result in 20dB/cm losses, our results are acceptable. It should be noticed that all the simulation assumes smooth metal surface which is not always the case and additional metal roughness can result in more losses. Furthermore, the simulation assumes text blood values for the metal permittivity, whereas in reality the metal loss is typically higher. This parameter can be checked separately, e.g. using elipsometry. The losses can be reduced by optimizing the fabrication process and reducing the roughness. Optimization can be achieved by modifying the etching process or smoothing of the metal mask.

7. Conclusion

In summary, we designed, simulated and experimentally demonstrated the fabrication and the measurements of a CMOS compatible LR-DLSPPW. We characterized the propagation length of the device and found it to be ~ 0.7mm. Owing to its promising characteristics of easy contact reach and good propagation length, the LR-DLSPPW can potentially become an important building block in future on-chip optoelectronic circuitry.

8. Future work

Our upcoming goals are to design, to fabricate and to characterize a thermo optic modulator based on the inherent ability to apply a current in the metal strip of the device, consequently heating the dielectric waveguide and change its effective refractive index. The phase modulator can be used in amplitude modulators such as Mach-zender and ring resonator. Another promising applications of plasmonic waveguide platform, is to perform an all optical modulation using 780nmFemtosecond pulsed laser illuminating the waveguide, resulting in an increase of the free carrier concentration inside the aluminum strip and the silicon. We want to illuminate the waveguide from the top, exploiting the fact that Si_3N_4 is

transparent at780nm wavelength, allowing to illuminate the Al and the silicon. It should be mentioned that there are two opposite effects in play, the increase of the free carrier concentration inside the aluminum will result in the amplification of the SPP [30-31] while the increase of the free carrier concentration inside the silicon will result in higher losses for the photons.

9. References

1. B. Jalali and S. Fathpour "Silicon photonics", *J. Lightw. Technol.*, vol. 24, no. 12, pp.4600 - 4615 2006

2. R. Soref, "The past, present and future of silicon photonics," IEEE J. Sel. Top. Quantum Electron. 12, 1687-1687 (2006)

3. G. K. Celler and S. Cristoloveanu, "Frontiers of silicon-on-insulator," J. Appl. Phys. 93, 4955-4978 (2003).

4. J. F. Buckwalter , J. Kim , X. Zheng , G. Li , K. Raj and A. Krishnamoorthy "A fully-integrated optical duobinary transceiver in a 130 nm SOI CMOS technology", Proc. IEEE Custom Integrated Circuits Conf. (CICC), pp.1 -4 (2011)

5. A. Biberman, S. Manipatruni, N. Ophir, L. Chen, M. Lipson, and K. Bergman, "First demonstration of long-haul transmission using silicon microring modulators," Opt. Express 18, 15544–15552 (2010)

6. M. T. Bohr, "Interconnect Scaling - the real limiter to high performance VLSI," Proceedings of IEDM, 1995.

7. K. Skadron et al., "Temperature-AwareMicroarchitecture," Proc. 30th Ann. Int'lSymp. Computer Architecture (ISCA 03),IEEE CS Press, 2003, pp. 2-13.

8. J. Schmidtchen, A. Splett, B. Shu&uml,ppert, and K. Petermann, "Low loss single mode optical waveguide with large cross-section in SOI", *Electron. Lett.*, vol. 27, no. 16, pp.1486 -1487 1991

9. J. Cardenas , C. B. Poitras , J. T. Robinson , K. Preston , L. Chen and M. Lipson "Low loss etchless silicon photonic waveguides", *Opt. Exp.*, vol. 17, no. 6, pp.4752 -4757 2009

10. H. Pan, S. Assefa, F. Horst, C. L. Schow, A. V. Rylyakov, W. M. J. Green, M. H. Khater, S. Kamlapurka, C.Reinholm, E. Kiewra, S. M. Shank, C. W. Baks, B. J. Offrein and Y. A. Vlasov," 250 Gbps 10-Channel WDM Silicon Photonics Receiver", Group IV Photonics (GFP), 2012 IEEE 9th International Conference, 162-164

11. X. Zheng, I. Shubin, G. Li, T. Pinguet, A. Mekis, J. Yao, H. Thacker, Y. Luo, J. Costa, K. Raj, J. E. Cunningham, and A. V. Krishnamoorthy, "A tunable 1x4 silicon CMOS photonic wavelength multiplexer/demultiplexer for dense optical interconnects," Opt. Express 18(5), 5151–5160 (2010)

12. Y.Ding, H. Ou, J. Xu, and C.Peucheret, "Silicon Photonic Integrated CircuitMode Multiplexer", IEEE photonics tech. lett. , 25(7)648-651 (2013)

13. P. Dong, W. Qian, H. Liang, R. Shafiiha, D. Feng, G. Li, J. E. Cunningham, A. V. Krishnamoorthy, and M. Asghari, "Thermally tunable silicon racetrack resonators with ultralow tuning power," Opt. Express 18(19), 20298–20304

14. Goykhman, B. Desiatov, S. Ben-Ezra, J. Shappir, and U. Levy, "Optimization of efficiency-loss figure of merit in carrier-depletion silicon Mach-Zehnder optical modulator," Opt. Express 21, 19518-19529 (2013).

15. E. Ozbay, "Plasmonics: Merging photonics and electronics at nanoscale dimensions", Science 311, 189-193 (2006).

16. B. Desiatov, I. Goykhman, and U. Levy, "Plasmonic nanofocusing of light in an integrated silicon photonics platform," Opt. Express19, 13150–13157 (2011)

17. D. K. Gramotnev and S. I. Bozhevolnyi, "Plasmonics beyond the diffraction limit", Nature Photonics 4, 83-91 (2010).

18. S. I. Bozhevolnyi, V. S. Volkov, E. Devaux, J.-Y. Laluet, and T. W. Ebbesen, "Channel plasmonsubwavelength waveguide components including interferometers and ring resonators," Nature, 440, 508-511 (2006).

19. J. A. Dionne, K. Diest, L. A. Sweatlock, and H. A. Atwater, "Plasmostor: A metal−oxide−Si field effect plasmonic modulator", Nano Letters 9, 897-902 (2009).

20. W. Cai, J. S. White, and M. L. Brongersma, "Compact, high-speed and power-efficient electrooptic plasmonic modulators", Nano Letters 9, 4403-4411 (2009).

21. Akbari, R. N. Tait, and P. Berini, "Surface plasmon waveguide Schottky detector," Opt. Express, 18, 8505-8514 (2010).

22. R. F. Oulton, V. J. Sorger, T. Zentgraf, R.-M. Ma, C. Gladden, L. Dai, G. Bartal, and X. Zhang, "Plasmon lasers at deep subwavelength scale", Nature 461, 629-632 (2009).

23. M. P. Nezhad, A. Simic, O. Bondarenko, B. Slutsky, A. Mizrahi, L. Feng, V. Lomakin, and Y. Fainman, "Room-temperature subwavelengthmetallo-dielectric lasers", NaturePhotonics 4, 395-399 (2010).

24. I.Goykhman, B. Desiatov, J. Khurgin, J. Shappir, and U. Levy, "Waveguide based compact silicon Schottky photodetector with enhanced responsivity in the telecom spectral band," Opt. Express 20, 28594-28602 (2012).

25. R. Charbonneau, N. Lahoud, G. Mattiussi, and P. Berini, "Demonstration of integrated optics elements based on long-ranging surface plasmonpolaritons", Opt. Express 13, 977-984 (2005).

26. T. Holmgaard, Z. Chen, S. I. Bozhevolnyi, L. Markey, A. Dereux, A. V. Krasavin, and A. V. Zayats, "Bend- and splitting loss of dielectric-loaded surface plasmon-polariton waveguides", Opt. Express 16, 13 585-13 592 (2008).

27. G. Veronis and S. Fan, "Bends and splitters in metal-dielectric-metal subwavelength plasmonic waveguides", Appl. Phys. Lett. 87, 131 102 (2005).

28. V. S. Volkov, S. I. Bozhevolnyi, E. Devaux, and T. W. Ebbesen, "Compact gradual bends for channel plasmonpolaritons", Opt. Express 14, 4494-4503 (2006).

29. A. Melikyan L. Alloatti, A. Muslija, D. Hillerkuss, P. C. Schindler, J. Li1, R. Palmer, D. Korn,S. Muehlbrandt, D. Van Thourhout, B. Chen, R. Dinu, M. Sommer, C. Koos, M. Kohl,W. Freudeand J. Leuthold, "High-speed plasmonic phase modulators", Nat. Photon., vol. 8, no. 3, pp.229 -233 2014

30. N. Rotenberg, M. Betz, and H. M. van Driel, “Ultrafast all-optical coupling of light to surface plasmonpolaritons on plain metal surfaces,” Phys. Rev. Lett. 105(1), 017402 (2010)

31. K. F. MacDonald, Z. L. Sámson, M. I. Stockman, and N. I. Zheludev, “Ultrafast active plasmonics,” Nat. Photonics 3(1), 55–58 (2009).

32. J. Homola, S. S. Yee, and G. Gauglitz,”Surface plasmon resonance sensor: review”, Sens. Actuators B 54, 3 (1999).

33. B. Schwarz, P. Reininger, D. Ristanic´, H. Detz, A. M. Andrews, W. Schrenk, G.Strasser,”Monolithically integrated mid-infrared lab-on-a-chip using plasmonics and quantum cascade structures”, Nature Communications 5, 4085,(2014)

34. R. Oulton, V. Sorger, D. A. Genov, D. F. P. Pile, X. Zhang, "A hybrid plasmonic waveguide for subwavelength confinement and long range propagation", Nature Photonics 2, (2008).

35. I.Goykhman, B. Desiatov, and U. Levy, "Experimental demonstration of locally oxidized hybrid silicon-plasmonic waveguide"

36. L. J. Zhou, X. M. Sun, X. W. Li, and J. P. Chen, “Miniature microring resonator sensor based on a hybrid plasmonic waveguide,” Sensors (Basel)11(7), 6856–6867 (2011).

37. G.Zhou, T. Wang, P. Cao, H. Xie, F. Liu, Y. Su, “Design of plasmon waveguide with strong field confinement and low loss for nonlinearity enhancement”, Group IV Photonics (GFP), 2010 7th IEEE International Conference, 69-71

38. X. Sun, L. Zhou, X. Li, Z. Hong, and J. Chen,” Design and analysis of a phase modulator based on ametal–polymer–silicon hybrid plasmonic waveguide”,Applied Optics, 50 (20), 3428-3434 (2011)

39. V. S. Volkov, Z. Han, M. G. Nielsen, K. Leosson, H. Keshmiri, J. Gosciniak, O. Albrektsen, and S. I. Bozhevolnyi, “Long-range dielectric-loaded surface plasmonpolariton waveguides operating at telecommunication wavelengths”, Opt. Lett. 36, 4278–4280 (2011).

40. T. Holmgaard, J. Gosciniak, and S. I. Bozhevolnyi, “Long-range dielectric-loaded surface plasmon-polaritonwaveguides”,Opt. Express 18(22), 23009–23015 (2010)

41. X. Shi, X. Zhang, Z. Han, U. Levy, and S. I. Bozhevolnyi, "CMOS-Compatible Long-Range Dielectric-Loaded Plasmonic Waveguides," J. Lightwave Technol. 31, 3361-3367 (2013).

42. Stefan A. Maier, “Plasmonics: Fundamentals and applications”,ISBN 0-387-33150-6

43. D. Sarid “Long-Range Surface-Plasma Waves on Very Thin Metal Films”,Phys. Rev. Lett. 47, 1927-1930 (1981).

44. Pinel. N, Bourlier. C, Saillard. J,“Degree of roughness of rough layers: extensions of the Rayleigh roughness criterion and some applications”, Prog. Electromagn. Res. B, 2010, 19, pp. 41–63

45. R. Y. Tsai, L. C. Kuo, and F. C. Ho, “Amorphous silicon and amorphous silicon nitride films prepared by plasma-enhanced chemical vapor deposition process as optical coating materials,” Appl. Opt. 32, 5561–5566 (1993).

46. Y. H. D. Lee and M. Lipson, “Back-End Deposited Silicon Photonics for Monolithic Integration on CMOS,” IEEE J. Sel. Top. Quantum Electron. vol. 19, no. 2, pp. 409–415, Mar. 2013.

47. KATSUNARI OKAMOTO, “Fundamentals of optical waveguides”, ISBN 13: 978-0-12-525096-2

48. G. T. Ruiter, “Near–field optical microscopy: Towards the molecular scale,” Ph.D. dissertation,University of Twente, The Netherlands, 1997, available from:**http://www.ub.utwente.nl/webdocs/tn/1/t0000001.pdf**.

49. F.P. Payne and J. P. R. Lacey, “A theoretical analysis of scattering loss from planar optical waveguides,” Optical and Quantum Electronics 26, 977-986 (1994).